nature portfolio

https://doi.org/10.1038/s41586-022-05424-3

Supplementary information

Traversable wormhole dynamics on a quantum processor

In the format provided by the authors and unedited

Supplementary information for "Traversable wormhole dynamics on a quantum processor"

CONTENTS

I. TRAVERSABLE WORMHOLE BEHAVIOR OF THE $N = 10$ SYK MODEL

A. Spectral properties

The energy spectra of SYK models with $q = 4$ and small values of $N \sim O(10)$ have been studied previously [1–4]. We have reproduced some of these results and extended them to our primary case of interest $N = 10$. Fig. S1 shows the normalized density of states $\rho(E)$ of the $N = 10$, 16, and 20 SYK models averaged over a large number of instantiations of the randomly selected couplings of the SYK Hamiltonian. As has been observed already in [3], for $N = 10$ the density of states exhibits some quasi-periodic behavior, which is attributed to level repulsion. In the large-N limit, the ground state energy is linear in N; as noted in [2], the finite-N SYK models approach this behavior very rapidly. This is shown in Fig. S2.

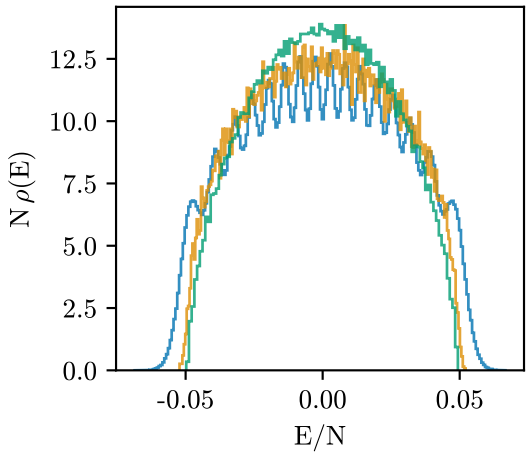

FIG. S1. Normalized density of states $\rho(E)$ of the N=10 (blue), $N = 16$ (orange), and $N = 20$ (green) SYK model averaging over 160,000/200/40 instantiations (respectively) of the randomly selected couplings in the SYK Hamiltonian.

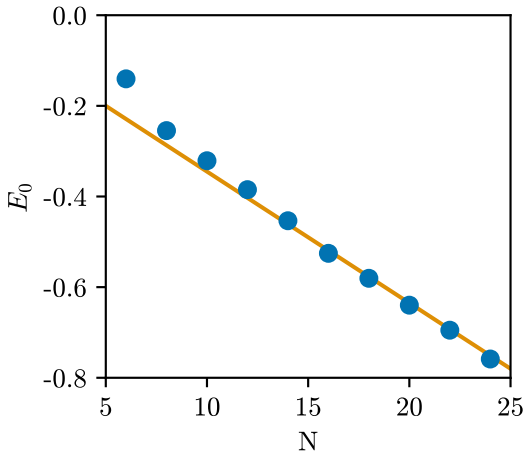

FIG. S2. Ground state energy of the SYK model, averaged over many instantiations, for N varying between 6 and 24. Also shown is the linear fit, $E_0 = -0.055 - 0.029N$, obtained in [1].

Following [1], we can examine short-range spectral correlations by computing the level spacing distribution $P(s)$, defined as the probability density to find

two energy eigenvalues separated by a distance s, in units of the mean eigenvalue spacing Δ, with no other eigenvalues in between. A characteristic feature of quantum chaotic systems is that $P(s)$, in the large-N limit, should take the Wigner form expected for random matrices:

$$P(s) = a_\beta \, s^\beta \, exp(-b_\beta \, s^2) \tag{S1}$$

where for $N = 10, 14, 18, \ldots$ the random matrices are drawn from the Gaussian Unitary Ensemble (GUE) with $\beta = 2$, $a_\beta = 32/\pi^2$, and $b_\beta = 4/\pi$.

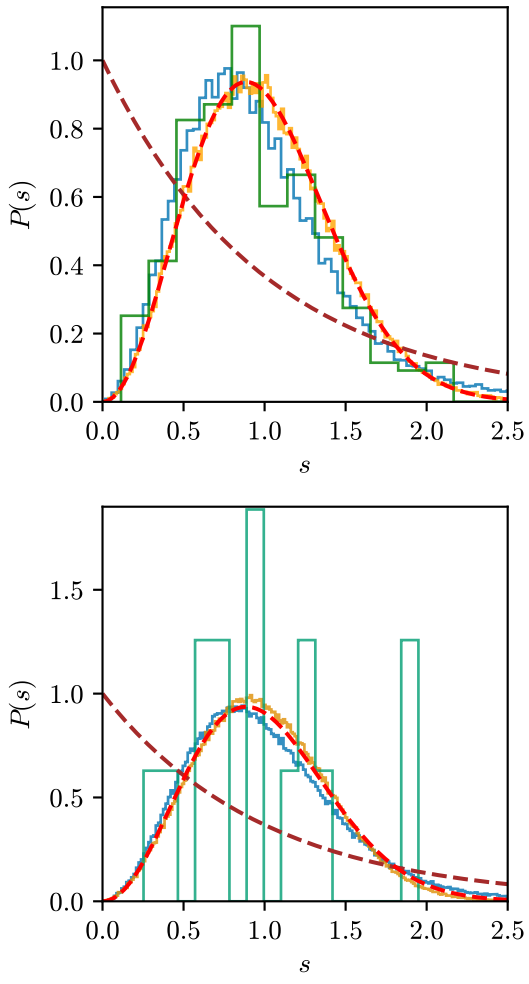

FIG. S3. Top: level spacing distribution $P(s)$ versus the separation of the eigenvalues s, for the SYK model with N=18 and mean level spacing $\Delta = 0.0046$. The blue histogram is averaging over 400 instantiations of the SYK Hamiltonian. The orange histogram is the same data "unfolded" by rescaling the spectrum such that the mean level spacing is the same for all energies. The green histogram is taken from a single instantiation of the SYK Hamiltonian. The red dashed line is the distribution expected in the large-N limit for random matrices from the Gaussian Unitary Ensemble. The brown dashed line is the expected behavior for a Poisson distribution. Bottom: same but for $N = 10$ and mean level spacing $\Delta = 0.091$.

A detailed comparison is shown in Fig. S3 for $N = 18$. The blue histogram, obtained by averaging over 400 instantiations, agrees with the GUE expectation, and the orange histogram, obtained by a rescaling described in [1, 5] as "unfolding," agrees even better. Furthermore, the green histogram shows the level spacing distribution for the 256 nondegenerate energy eigenvalues of a single instantiation of the SYK Hamiltonian, which also shows reasonable agreement. This is an example of a general property observed in all of the dynamics that we have studied relevant to traversable wormholes: the qualitative properties are present in single instantiations of the SYK Hamiltonian, rather than "emerging" from ensemble averages. Fig. S3 also shows the same kind of data for N=10; the behavior of single instantiations is coarser since there are 16 nondegenerate eigenvalues.

B. Scrambling and thermalization

In the large-N limit of the SYK model, the thermalization and scrambling behavior is well-studied [6]; we examine the $N = 10$ SYK model here (Fig. S4).

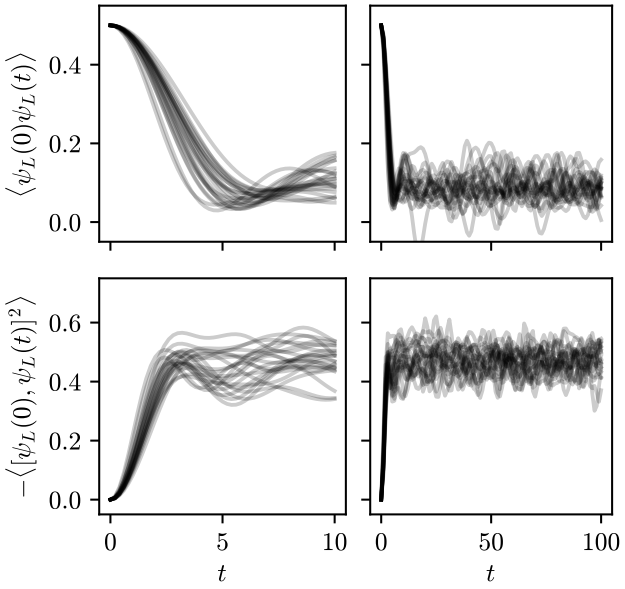

FIG. S4. Thermalization (top) and scrambling (bottom) of many instantiations of the $N = 10$ SYK Hamiltonian for small (left) and large (right) time scales at $\beta = 4$. Unlike in the large-N limit, the scrambling and thermalization times are approximately equal.

The thermalization (or dissipation) time t_d is given by the exponential decay of the two-point expectation value $\langle\psi(0)\psi(t)\rangle_\beta$. For a strongly coupled system, we expect $t_d \sim \beta$. Similarly, the out-of-time-order correlator $-\langle[\psi(0), \psi(t)]^2\rangle_\beta$ provides a scrambling time $t_* \sim \frac{\beta}{2\pi} \log N$. Hence, a large-$N$ SYK model satisfies $t_* \gg t_d$. Due to the small-N regime of our system, we instead observe $t_* \sim t_d$, which is compatible with wormhole-like teleportation but outside the usual scope of literature. Moreover, the precise

scrambling/thermalization times are not clearly defined. At large times, we confirm that the $N = 10$ Hamiltonian does not exhibit any pathological behavior, but rather continues to oscillate in the fully scrambled/thermalized regimes.

C. Interaction sign asymmetry

The Majorana SYK model with $N = 10$ fermions and Gaussian-distributed coefficients produces asymmetric mutual information dynamics with respect to the sign of the coupling interaction μ, as shown in Fig. 2 of the main text. To reasonably accommodate both limits of low-temperature and $J\beta < N$ for coefficient variance set by $J^2 = 2$, we choose $\beta = 4$. In Fig. S5, the population of $N = 10$ SYK models illustrated in Fig. 2 is shown exclusively for visual clarity.

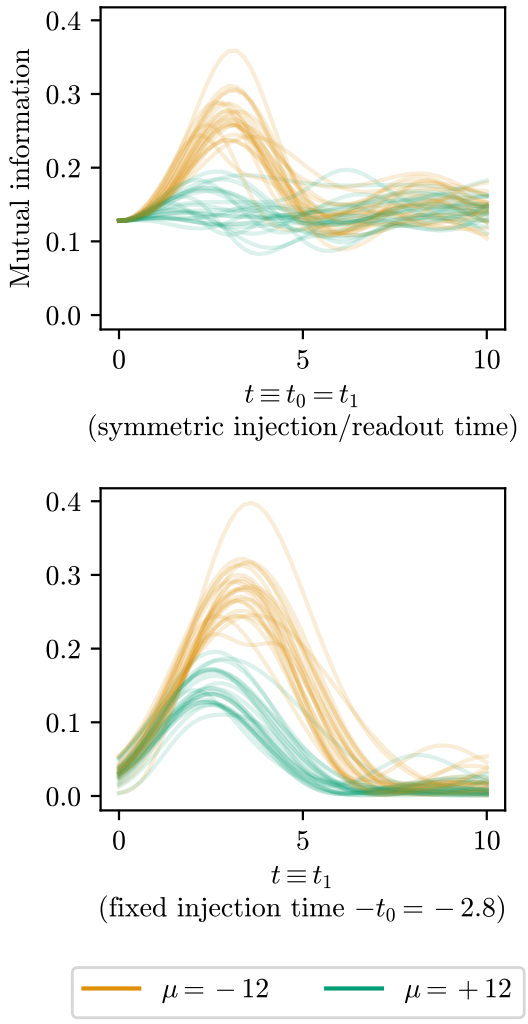

FIG. S5. Population of $N = 10$ SYK models with independently and identically distributed Gaussian coefficients. The mutual information is expected to peak around the scrambling time for $\mu < 0$ due to a negative energy shockwave rendering the wormhole traversable.

D. Time ordering

Due to the causal pathway provided by the smooth semiclassical geometry of a traversable wormhole, signals that travel through the wormhole follow first-in-first-out time-ordering: injecting a qubit later will cause it to emerge at a later time. Outside the appropriate window of time corresponding to wormhole teleportation, scrambling causes time-inverted teleportation to occur (Fig. 1b of the main text). Here we verify that the $N = 10$ SYK model exhibits wormhole-like behavior in the sense of causal time ordering within a certain window of injection times $-t_0$.

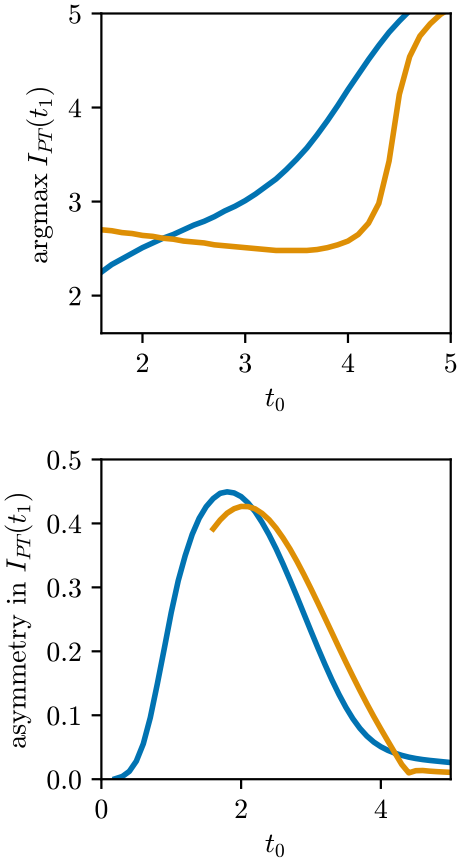

FIG. S6. Top: the arrival time, defined as argmax $I_{PT}(t_1)$, as a function of the magnitude t_0 of the injection time, for an instantaneous interaction (blue) with $\mu = -24$ and a Trotterized interaction (orange) with $\mu' = -10$ and $t_\mu/2 = 1.6$. Bottom: for given values of t_0 and arrival times as defined above, the asymmetry in the mutual information between negative and positive values of the interaction strength is plotted for the instantaneous interaction (blue) and the Trotterized interaction (orange).

In the teleportation protocol, the interaction $e^{i\mu V}$ happens instantaneously at time $t = 0$. Similarly to the learned Hamiltonian shown in Fig. 3f of the main text, an instantaneous interaction causes signals to approach the time-ordered behavior for a fixed window of time around $t_0 \approx 3$, where the wormhole-like behavior is strongest. This result may be interpreted

as the coexistence of teleportation by scrambling and the signal traversing through the wormhole. To exaggerate the effect, we can apply the interaction $e^{i\mu V}$ over a period $t \in [-t_\mu/2, t_\mu/2]$. Trotterizing the interaction in three steps of $e^{i\mu' V}$ applied at times $t = -t_\mu/2, 0, t_\mu/2$, we find that the time-ordered teleportation dominates the time-inverted teleportation. This is illustrated in Fig. S6. For a given value of the injection time $-t_0$, we define the arrival time as the time when the mutual information is maximal. The top figure shows that for the Trotterized interaction there is a finite window of injection time that exhibits the causal time ordering, whereas injecting too early (large t_0) produces inverted time ordering. The bottom figure demonstrates that Trotterizing the interaction does not diminish the interaction sign asymmetry characteristic of wormhole teleportation.

E. Analytic double-scaled limit

The exact gravitational dual of the SYK model is not known, but in the large-N and low-temperature limit, the correlation functions of SYK fermions agree with the boundary values of fermions propagating in a two-dimensional spacetime interacting at leading order by Jackiw-Teitelboim gravity. Quantum corrections in the gravity description are controlled by $\beta J/N$, whereas higher temperatures and q^2/N lead to interactions outside this minimal gravity sector. Such inelastic effects reduce the amplitude for on-shell transmission through the wormhole in a way that remains calculable at large N, although it is not known how to interpret them in the gravity language.

We provide evidence showing that wormhole-like behavior in a small-N system is theoretically well-motivated. The condition that $N \gg q \gg 1$, which led to drastic simplifications in [7], is difficult to achieve in small-N systems. Alternatively, Ref. [8] considered a large-N limit where q^2/N is fixed. This "double-scaled" limit is more suitable for studying small-N systems, where a large hierarchy between N and q cannot be maintained. As explained in [8], moments of the Hamiltonian $\mathrm{Tr}\, H^{2n}$, $n \in \mathbb{N}$ may be computed in the double-scaled limit as a sum over chord diagrams with $2n$ external vertices. Each chord diagram represents one of the $(2n-1)!!$ ways of Wick-contracting the $J_{j_1 \ldots j_q}$ parameters that define the Hamiltonian. The chord diagrams may be resummed to obtain a compact analytic expression that takes the form of an integral. Low-point correlators may be computed in a similar fashion, yielding a low-dimensional integral that may be evaluated numerically.

By numerically integrating the analytic predictions of [8] for correlators in the double-scaled SYK model, we find wormhole-like behavior that qualitatively agrees with behavior shown in the main text. In particular, we numerically evaluate the correlators

$$c_1 = \left\langle \{\psi_L^1, [\psi_L^2, U^\dagger \psi_R^1 \psi_R^2 U]\} \right\rangle$$
$$c_2 = \left\langle \{\psi_L^1, U^\dagger \psi_R^1 U\} \right\rangle$$
$$c_3 = \left\langle \{\psi_L^2, \psi_L^1 U^\dagger \psi_R^2 U \psi_L^1\} \right\rangle,$$

which are sufficient to compute the mutual information under $SO(N)$ symmetry, as described in the following section (Eq. S4). Here, $U = e^{i\mu V}$ represents the interaction. We evaluate the correlators in a power series in μ and compute the individual terms, up to a sufficiently high order, using the results of [8].

Our results for the mutual information as a function of t_1 for fixed t_0 are shown in Fig. S7. The results show an asymmetry for opposite signs of μ, demonstrating qualitative agreement with numerical simulation of the $N = 10$ SYK model. While the analytic results of [8] are only strictly correct in the double-scaled limit, we can extrapolate them to small N to qualitatively predict wormhole behavior in a practically sized system.

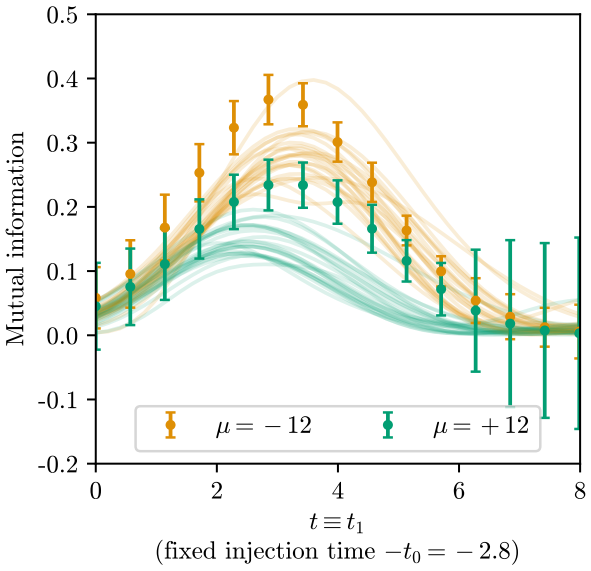

FIG. S7. Mutual information over time in the double-scaled SYK model, with $N = 10$, $\beta = 4$, and $q = 4$ (dots) and numerical simulation of $N = 10$ SYK models (lines). The asymmetric time-dependence for opposite values of μ agrees qualitatively and gives similar peak positions and heights compared to numerical simulation. The error bars represent uncertainty from the numerical integration of the analytic expressions.

II. DYNAMICS OF THE LEARNED SPARSE SYK MODEL

A. Eternal traversable wormhole

In Fig. 3f of the main text, we demonstrated that causal time-ordering is achieved through the Trotterization of the interaction $e^{i\mu V}$. This interpolates between the instantaneous interaction of the protocol

by Gao and Jafferis [7] and the eternal traversable wormhole protocol of Maldacena and Qi [9], which time-evolves the system over the full Hamiltonian

$$H_{\text{tot}} = H_L + H_R + \mu_{\text{MQ}} H_{\text{int}} \tag{S2}$$

where $H_{\text{int}} \equiv i \sum_j \psi_L^j \psi_R^j$ implements the interaction operator V, and μ_{MQ} is a rescaled version of the coupling strength μ. Specifically, since the wormhole is eternal, the only relevant timescale is $t_{\text{transit}} = t_0 + t_1$. The Maldacena-Qi coupling is related to our standard coupling μ by $\mu_{\text{MQ}} t_{\text{transit}} = -\mu/(qN)$.

We examine further gravitational behavior of the learned Hamiltonian within the eternal traversable wormhole protocol in the following setup. At time $-t_0$, a qubit q_l is swapped into the left side of the wormhole, entangled with a reference qubit. Simultaneously, a qubit q_r is swapped into the right side of the wormhole. At time t_1, the mutual information between the reference and the right side (where q_l was teleported to) is measured. In gravitational variables, the presence of q_r should delay the arrival of the signal travelling left to right due to a Shapiro time delay from scattering in the bulk. We observe this behavior in the learned Hamiltonian (Fig. S8) (reproduced from Fig. 3e of the main text).

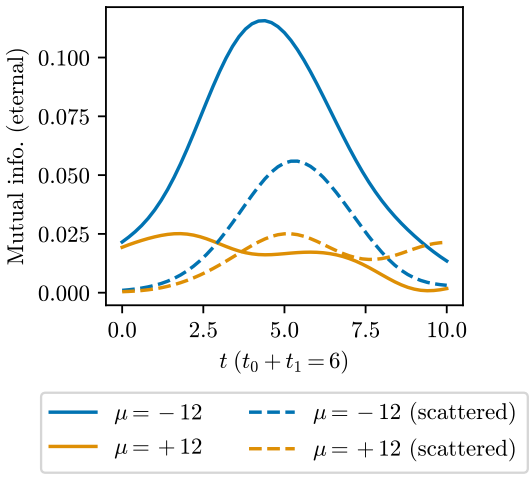

FIG. S8. Mutual information in the eternal traversable protocol with a single qubit injected from the left (solid) or both a qubit injected from the left and the right to cause scattering in the bulk (dashed). The left signal emerges on the right side of the wormhole at a later time when there exists an additional qubit traversing the wormhole, as seen by the peak shifting to the right. A similar Shapiro time delay is observed when the site of the qubit swapped into the right system is changed (not shown here).

B. High-temperature and non-gravitational behavior

We evaluate the dynamics of the learned Hamiltonian outside the gravitationally meaningful regime. We recover symmetric teleportation with respect to μ in the high-temperature regime, as expected for a traversable wormhole protocol [7]. We also evaluate the dynamics for different values of coupling μ and observe similarities to the full SYK model.

In Fig. S9, we examine the mutual information for μ and β that do not produce the peaked signature of through-the-wormhole teleportation. The similarities in mutual information behavior suggest the effective sparse Hamiltonian has dynamics resembling that of the original SYK Hamiltonian. At early times, direct swapping causes nonzero mutual information due to the interaction occurring before the injected qubit has thermalized through the left system. Explicitly, for $t \equiv t_0 = t_1$, the two-point function $\langle \psi(t)\psi(0) \rangle$ does not decay sufficiently, causing the interaction $e^{i\mu V}$ to directly send the qubit from the left to the right system. This behavior exists when μ, β are chosen to maximize through-the-wormhole teleportation; however, by the time of the wormhole teleportation signal ($t \approx 2.8$), the fake signal decays due to thermalization. For other choices of μ, β, direct swapping becomes the dominant signal (Fig. S9). We note that a direct swap is independent of both the sign of μ and the state.

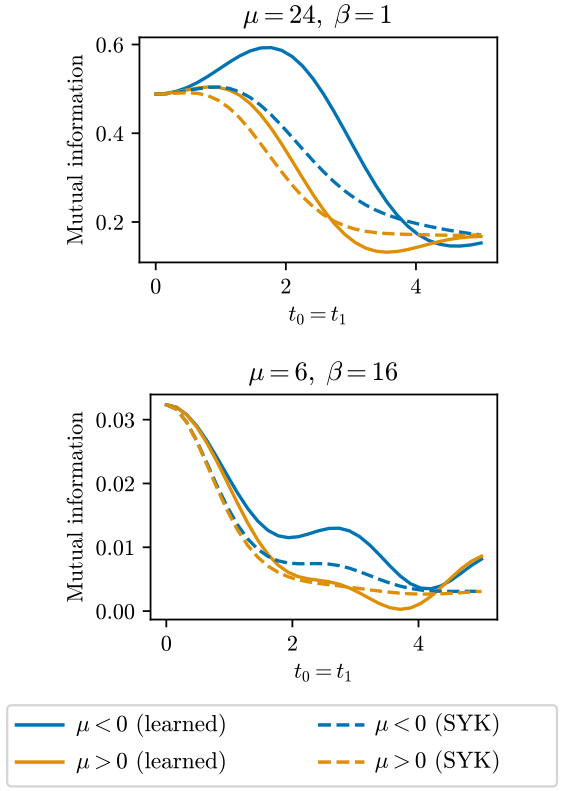

FIG. S9. Mutual information for different values of coupling strength μ and inverse temperature β.

In the high-temperature limit, the asymmetry in mutual information between $\mu > 0$ and $\mu < 0$ is expected to decrease due to the disappearance of low-temperature geometric teleportation and the dominance of fully scrambled dynamics that cause non-gravitational teleportation. For the wormhole proto-

col, this high-temperature teleportation corresponds to the interference regime [7, 10, 11], where the left-right correlation function $\mathcal{K}$ (Eq. S5) is nonzero. More generally, chaotic systems such as GUE ensembles, random circuits, and spin chains exhibit such high-temperature teleportation [12, 13]. We verify that high-temperature teleportation occurs with reduced asymmetry in the sign of μ. We find that some residual asymmetry remains at infinite temperatures due to the small-N approximation of the SYK model. This minor asymmetry agrees between the learned Hamiltonian and the $N = 10$ SYK model.

As the temperature increases (i.e., $\beta \to 0$), the mutual information asymmetry is observed to decrease as expected; moreover, the reduced mutual information asymmetry of the learned model agrees with that of the $N = 10$ SYK model (Fig. S10). We conclude that the learned model preserves the high-temperature dynamics of the SYK model.

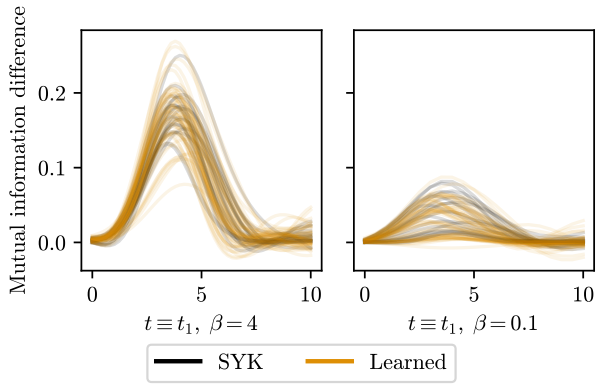

FIG. S10. Mutual information difference ($I_{\mu<0} - I_{\mu>0}$) for fixed $-t_0 = -2.8$ evaluated at $\beta = 4$ (left) and $\beta = 0.1$ (right) for a population of learned Hamiltonians and SYK models.

We note that the mutual information asymmetry at infinite temperature does not vanish entirely due to a small-N correction. To demonstrate this, we evaluate the mutual information I_{PT} in terms of the density matrix elements and compare it to the computation in terms of the left-right propagator $\mathcal{K}$, following the results of Ref. [7]. The density matrix ρ_{PT} at the end of the protocol is expressed in terms of correlation functions over Dirac fermions obtained by pairing Majorana fermions: $\chi_{L,R} = (\psi^1_{L,R} + i\psi^2_{L,R})/\sqrt{2}$. Explicitly, letting $U = e^{i\mu V}$, define matrix elements

$$\begin{aligned}
\rho_{11} &= \langle \chi_L \chi_L^\dagger U^\dagger \chi_R \chi_R^\dagger U \chi_L \chi_L^\dagger \rangle + \langle \chi_L^\dagger U^\dagger \chi_R \chi_R^\dagger U \chi_L \rangle \\
\rho_{14} &= \langle \chi_L U^\dagger \chi_R^\dagger U \chi_L \chi_L^\dagger \rangle + \langle \chi_L^\dagger \chi_L U^\dagger \chi_R^\dagger U \chi_L \rangle \\
\rho_{22} &= \langle \chi_L U^\dagger \chi_R \chi_R^\dagger U \chi_L^\dagger \rangle + \langle \chi_L^\dagger \chi_L U^\dagger \chi_R \chi_R^\dagger U \chi_L^\dagger \chi_L \rangle \\
\rho_{23} &= \langle \chi_L \chi_L^\dagger U^\dagger \chi_R^\dagger U \chi_L^\dagger \rangle + \langle \chi_L^\dagger U^\dagger \chi_R^\dagger U \chi_L^\dagger \chi_L \rangle \\
\rho_{33} &= \langle \chi_L \chi_L^\dagger U^\dagger \chi_R^\dagger \chi_R U \chi_L \chi_L^\dagger \rangle + \langle \chi_L^\dagger U^\dagger \chi_R^\dagger \chi_R U \chi_L \rangle \\
\rho_{44} &= \langle \chi_L U^\dagger \chi_R^\dagger \chi_R U \chi_L^\dagger \rangle + \langle \chi_L^\dagger \chi_L U^\dagger \chi_R^\dagger \chi_R U \chi_L^\dagger \chi_L \rangle.
\end{aligned}$$

The density matrix is then given by

$$\rho_{PT} = \frac{1}{2}\begin{pmatrix} \rho_{11} & 0 & 0 & \rho_{14} \\ 0 & \rho_{22} & \rho_{23} & 0 \\ 0 & \rho_{23}^* & \rho_{33} & 0 \\ \rho_{14} & 0 & 0 & \rho_{44} \end{pmatrix} \tag{S3}$$

$$\xrightarrow[SO(N)]{} \frac{1}{2}\begin{pmatrix} \rho_{11} & 0 & 0 & \rho_{14} \\ 0 & 1-\rho_{11} & 0 & 0 \\ 0 & 0 & 1-\rho_{11} & 0 \\ \rho_{14} & 0 & 0 & \rho_{11} \end{pmatrix}, \tag{S4}$$

where the limit occurs by applying the $SO(N)$ symmetry of the ensemble average of the SYK model to simplify the exchange of indices (i.e., invariance under $\psi^1_{L,R} \leftrightarrow \psi^2_{L,R}$). This simplification yields mutual information expressed only in terms of matrix elements

$$\begin{aligned}
\rho_{11} &= \frac{1}{2}\left[1 - \left\langle \{\psi^1_L, [\psi^2_L, U^\dagger \psi^1_R \psi^2_R U]\} \right\rangle\right] \\
\rho_{14} &= \frac{1}{2}\left\langle \{\psi^1_L, U^\dagger \psi^1_R U\} \right\rangle - \left\langle \{\psi^2_L, \psi^1_L U^\dagger \psi^2_R U \psi^1_L\} \right\rangle.
\end{aligned}$$

We must apply a large-N approximation to express ρ_{PT} in terms of the left-right propagator $\mathcal{K}$, defined by

$$\mathcal{K}(t,t') = \langle \{\psi_L(-t'), \mathcal{U}^\dagger \psi_R(t) \mathcal{U}\} \rangle. \tag{S5}$$

As given in (4.6) of Ref. [7], the individual correlation functions factorize up to $O(1/N)$ corrections, e.g.,

$$\left\langle \{\psi^1_L(-t'), [\psi^2_L(-t'), U^\dagger \psi^1_R(t) \psi^2_R(t) U]\} \right\rangle \approx -\mathcal{K}(t,t')^2$$

up to $O(1/N)$ error. This gives matrix elements

$$\rho_{11} = \frac{1}{2}(1 + \mathcal{K}(t,t')^2), \quad \rho_{14} = \mathcal{K}(t,t'), \tag{S6}$$

yielding von Neumann entropy

$$\begin{aligned}
I_{PT} = &\frac{1}{4}[(\mathcal{K}-1)^2 \log(\mathcal{K}-1)^2 + (\mathcal{K}+1)^2 \log(\mathcal{K}+1)^2 \\
&+ 2(1-\mathcal{K}^2)\log\big(1-\mathcal{K}^2\big)].
\end{aligned} \tag{S7}$$

We evaluate the mutual information for all three levels of approximation (Fig. S11): the exact mutual information (computed from Eq. S3, evaluated by swapping a qubit into the wormhole following the full protocol format), the ensemble-averaging approximation (computed from Eq. S4), and the combined large-N and $SO(N)$ approximation in terms of $\mathcal{K}$ (Eq. S7).

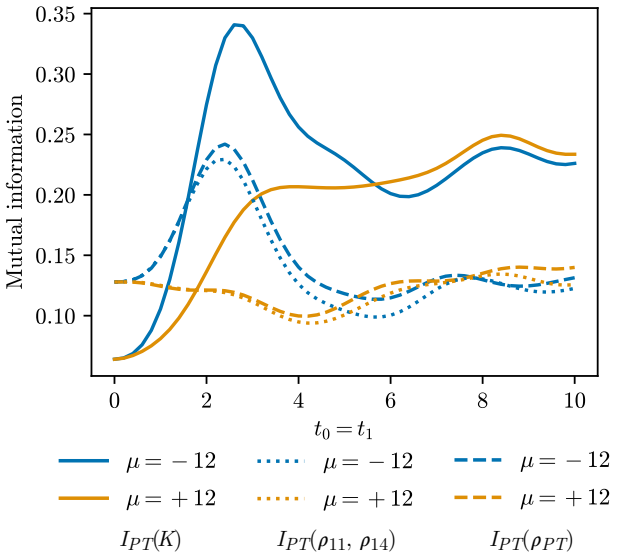

FIG. S11. Mutual information of the $N = 10$ SYK model for fixed $-t_0 = -2.8$ evaluated according to three levels of approximation (left to right in legend): the large-N limit and $SO(N)$ ensemble average from Eq. S7, the $SO(N)$ approximation from Eq. S4, and the exact mutual information from Eq. S3.

While the mutual information is asymmetric in μ for $\beta = 0$ under the exact computation, we confirm that both the learned Hamiltonian and SYK models become perfectly symmetric according to the $\mathcal{K}$ computation (Eq. S7) in the infinite-temperature limit (Fig. S12). This shows that the learned Hamiltonian satisfies the high-temperature behavior expected of the SYK model, up to similar $O(1/N)$ corrections.

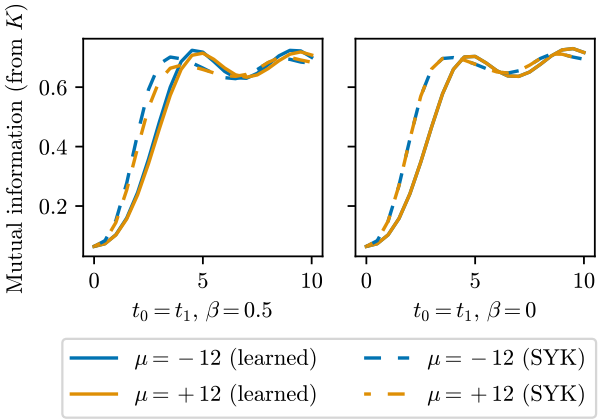

FIG. S12. Mutual information for fixed $-t_0 = -2.8$ evaluated at $\beta = 0.5$ (left) and $\beta = 0$ (right) for the learned Hamiltonian and original SYK Hamiltonian. The asymmetry in μ disappears at $\beta = 0$; the $\mu = +12$ and $\mu = -12$ lines exactly overlap.

III. SIZE WINDING

A. Overview

We review and extend the size winding framework following Refs. [12] and [13].

Given thermal state $\rho_\beta = e^{-\beta H}/\operatorname{tr} e^{-\beta H}$ and time-evolved operator $\psi^1(t)$ under the single-sided Hamiltonian H_L, consider the decomposition $\rho_\beta^{1/2}\psi^1(t) = \sum_P c_P(t)\psi^P$ for $P \in \{0,1\}^n$ over strings of $|P|$ fermions, where each P_i indicates if the compound fermionic operator has a fermion on site i. The property of size winding refers to the phase of c_P^2 with linear dependence on $|P|$,

$$c_P = e^{i(\alpha|P|/N+\phi)} r_P,\ r_P \in \mathbb{R}, \tag{S8}$$

where r_P may be positive or negative.

This ansatz is satisfied exactly in "perfect" (or undamped) size winding, which provides a necessary fine-grained property of quantum systems with a nearly-AdS_2 bulk, describing holographic behavior [13]. In general, for an observer acting on the left,

$$\frac{1}{2^{n/2}} O_L^T(-t)\,|\mathrm{TFD}\rangle = \rho_\beta^{1/2} O_R(t)\,|I\rangle \tag{S9}$$

is satisfied, where $|I\rangle$ is the maximally entangled state (i.e., $(\psi_L^j + i\psi_R^j)\,|I\rangle = 0$ for all j) and $O(t) = e^{iHt}Oe^{-iHt}$. When acting on the right system, we have

$$\frac{1}{2^{n/2}} O_R(t)\,|\mathrm{TFD}\rangle = O_R(t)\rho_\beta^{1/2}\,|I\rangle\,. \tag{S10}$$

Applying the perfect size winding ansatz, we get

$$O_L^T(-t)\,|\mathrm{TFD}\rangle = \sum_P e^{i\alpha|P|/N} r_P\,|P\rangle \tag{S11}$$

$$O_R(t)\,|\mathrm{TFD}\rangle = \sum_P e^{-i\alpha|P|/N} r_P\,|P\rangle\,, \tag{S12}$$

where $|P\rangle = \psi_R^P\,|I\rangle$. The action of the observables $O_L^T(-t)$ and $O_R(t)$ are equal up to the direction of the winding phase $\alpha|P|/N$.

To consider all operators of a given size, it is convenient to consider the winding size distribution

$$q(l) = \sum_{|P|=l} c_P^2. \tag{S13}$$

The effect of the interaction on the winding size distribution $q(l)$ may be determined by applying $e^{i\mu V}$ to a basis of states $|P\rangle$. The interaction offsets the phase $e^{i\mu V}\,|P\rangle = e^{i\mu|P|/4n}\,|P\rangle$ up to a constant [12, 14]. Since we may expand in the basis of $|P\rangle$, the interaction causes a phase offset proportional to the coupling μ.

The phase of $q(l)$ corresponds to the position of the infalling particle, while the magnitude of $q(l)$ provides

the particle's momentum. Similarly to the definition in Eq. 12 of [12], we consider the Fourier transform

$$\tilde{q}(x) = \sum_l q(l) e^{-ixl/4N}, \tag{S14}$$

which provides the bulk location. Introducing the interaction shifts x. For a properly chosen value of μ, this kicks the particle to the other side of the horizon. The consequent reversal of size winding direction is seen by the flipped slope of $\arg q(l)2$ shown in Fig. 3d of the main text. The location of the black hole horizon is determined by the bulk location of $\arg q(l)$ with zero slope.

It has been shown that systems exhibiting gravitational teleportation must demonstrate near-perfect size winding, including the SYK model for $N \gg q \gg 1$. While a maximal Lyapunov exponent of the OTOC is an equivalent signature in the large-N limit [6], size winding remains well-defined for small-N systems. Moreover, perfect size winding provides a strict criterion that distinguishes geometric teleportation from other teleportation mechanisms, as summarized below.

- Low-temperature through-the-wormhole transmission: perfect size winding occurs, causing teleportation around the scrambling time. This holds for large-q, large-N SYK models and systems dual to nearly-AdS_2. Teleportation shows strong dependence on the sign of μ.

- Low-temperature non-geometric transmission: imperfect size winding occurs, causing teleportation around the scrambling time. This holds for non-gravitational systems, including random non-local Hamiltonians. Teleportation shows dependence on the sign of μ. Due to the absence of k-locality, low-temperature states of random Hamiltonians still access an $O(1)$ fraction of the Hilbert space instead of an exponentially small fraction.

- High-temperature teleportation: no size winding, but teleportation occurs at times larger than the scrambling time due to random dynamics. Many systems, including chaotic spin chains and random circuits, teleport through state transfer. Teleportation shows no dependence on the sign of μ.

There is strong evidence that perfect size winding is a sufficient criterion for a gravitational dual [12, 13, 15].

B. Perfect size winding of the sparse SYK model

The sparsification algorithm optimizes the tradeoff between reducing the number of terms in the Hamiltonian and preserving the asymmetry in μ of the mutual information, i.e., the teleportation signal. Although we did not include perfect size winding in the optimization loss function, the resulting Hamiltonian satisfies this property: the most straightforward mechanism to create a strong asymmetry in μ is by enforcing perfect size winding.

Before examining size winding, we verify the growth of ψ^1 through the system by showing that the magnitude of coefficient c_1 decreases over time (Fig. S13). Simultaneously, coefficients corresponding to operators of larger size increase.

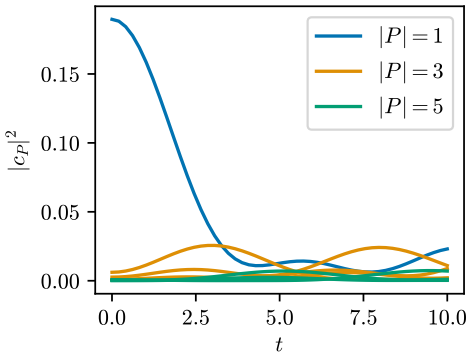

FIG. S13. Growth of single fermion (size 1) into larger-size operators under time evolution by the learned sparse Hamiltonian at $\beta = 4$. The degeneracy of nonzero c_P causes multiple c_P coefficients (Eq. S8) for the same size $|P|$.

The linear dependence of $q(l)$ on operator size l is shown in Fig. 3d of the main text. We recall that at early times ($t = 0$), the slope of $q(l)$ is larger than at the time of teleportation ($t = 2.8$). By Eq. S14, this behavior corresponds to the infalling particle starting further away from horizon and approaching the horizon before traversing the wormhole.

We characterize the size winding as perfect by checking the ratio of the winding size distribution to the conventional size distribution:

$$\frac{\left|\sum_{|P|=l} c_P^2\right|}{\sum_{|P|=l} |c_P|^2} = 1. \tag{S15}$$

The sum over all coefficients of identical size, if the phase of each coefficient c_P only depends on size (Eq. S8), will not be affected by destructive interference of phases. As shown in Fig. S14, the equality is nearly saturated by the learned Hamiltonian at the time of teleportation.

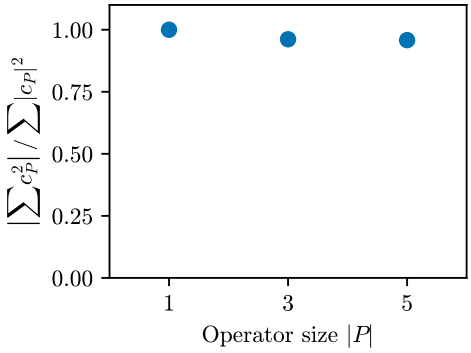

FIG. S14. Ratio of winding size distribution $q(l)$ and the conventional size distribution $\sum |c_P|^2$ at $\beta = 4$ and $t = 2.8$. The ratio is approximately unity, showing that the phases of the individual c_P coefficients aligned in the manner of perfect size winding.

The interaction causes the phases to rotate below the horizontal, crossing the horizon. A stronger negative energy interaction causes further rotation, as shown in Fig. S15. In the main text, we use an interaction coupling $\mu = -12$ that is preserved from the original SYK model. An optimal interaction causes the magnitude of the winding slope to remain unchanged. We show in the next section that $\mu \approx -12$ is indeed optimal for the full SYK model. For the learned Hamiltonian, μ can be tuned to optimize size winding (Fig. S15), which produces a stronger teleportation signal (Fig. S16). To cross the horizon and traverse the wormhole, $\mu = -12$ is sufficient.

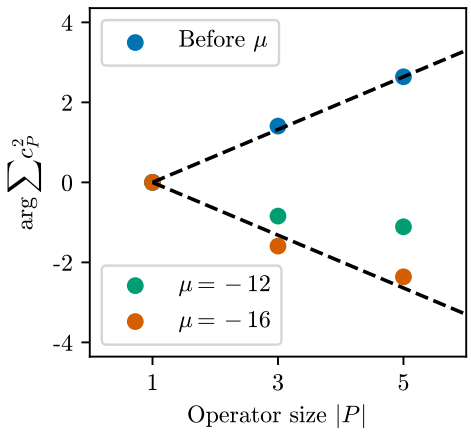

FIG. S15. Size winding before and after interaction at $t = 2.8$ for different values of μ at $\beta = 4$. Perfect size winding with equal magnitude of slope before and after the interaction (black dashed line) is best satisfied for the choice of interaction coupling $\mu \approx -16$.

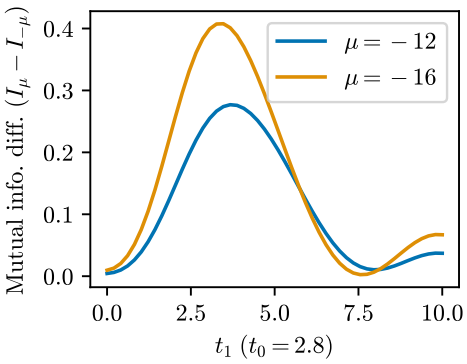

FIG. S16. Dependence of mutual information dynamics on coupling μ at $\beta = 4$. The signal is strengthened at $\mu = -16$, as is consistent with the size winding picture.

We note that perfect size winding occurs in the zero-temperature ground state, producing slope $\pi/2$ for reasons independent of gravity. We find that $\beta = 4$ is sufficiently far from zero temperature, as seen by the values of the phases. We calculate the thermal state overlap with the ground state to be 0.52. We calculate in the original SYK model the corresponding overlap to be 0.38.

C. Fragility of perfect size winding

We compare the presence of perfect size winding in the learned Hamiltonian to a) suboptimal sparsification of the SYK model, b) the SYK model, and c) the Gaussian unitary ensemble.

In the training process, the loss function penalizes the norm of Hamiltonian terms to induce sparsification. This regularization is enforced during gradient descent, with the norms of terms being gradually reduced in a manner that consistently preserves the asymmetric mutual information dynamics with respect to the interaction coupling μ. We now consider a more naive form of sparsification. Instead of removing terms from the Hamiltonian in an optimized fashion until 5 terms remain, the largest 5 terms of the initial SYK Hamiltonian are kept and all remaining terms are removed. The coefficients of those 5 largest terms are then optimized to match the original SYK model's mutual information dynamics. Under this modified sparsification procedure, mutual information dynamics are degraded (Fig. S17). Moreover, perfect size winding is lost (Fig. S18).

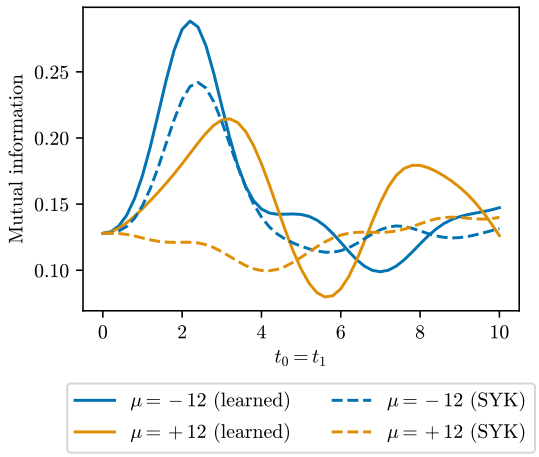

FIG. S17. Comparison of mutual information dynamics of the modified (suboptimal) sparsified Hamiltonian and SYK Hamiltonian.

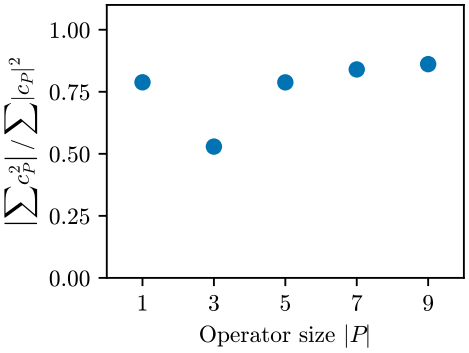

FIG. S19. Ratio of winding size distribution to the conventional size distribution at $\beta = 4$. We show the SYK Hamiltonian used to initialize training of the learned Hamiltonian in the main text.

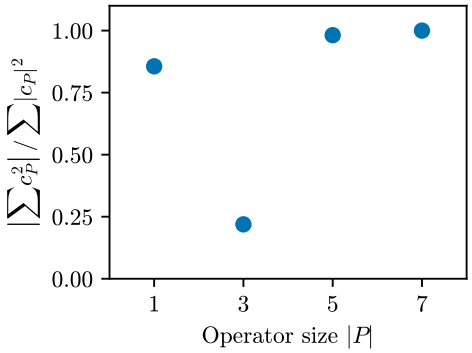

FIG. S18. Ratio of winding size distribution to the conventional size distribution at $\beta = 4$. The ratio should be approximately 1 for all $|P|$ to satisfy perfect size winding.

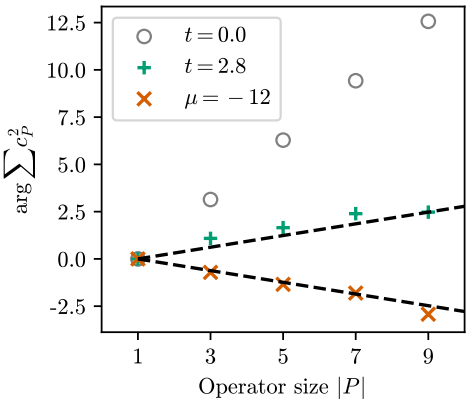

FIG. S20. Size winding of the SYK Hamiltonian as a function of operator size. We show the SYK Hamiltonian used to initialize training of the learned Hamiltonian in the main text.

The SYK model is known to exhibit perfect size winding in the low-temperature, large-q, large-N limit with $q^2 \ll N$, where teleportation is perfect due to completely elastic behavior. In the $N = 10$, $q = 4$ SYK model studied above, inelastic effects that reduce the teleportation signal signify that the dual is not pure Einstein/JT gravity. The teleportation signal remains dominated by a Shapiro advance in the gravity description of the dual. The inelastic effects, numerically confirmed by the chord diagram computation, damp the size winding (Fig. S19). Nevertheless, the slope of $q(l)$ depends linearly on l; it decreases and then reverses as the infalling particle approaches then crosses the horizon (Fig. S20). For the SYK model, the choice of $\mu = -12$ is seen to optimally satisfy the teleportation by size mechanism, reversing the size winding direction without affect its speed.

Besides the SYK model, we compare the size winding of the learned Hamiltonian to size winding of the Gaussian unitary ensemble (GUE). The presence of imperfect size winding of the GUE, as expected by Ref. [13], suggests that it should generate some asymmetry in mutual information for $\mu < 0$ compared to $\mu > 0$. We confirm this behavior with the wormhole teleportation protocol: $I_{\mu<0}$ exceeds $I_{\mu>0}$ with peak-like behavior (Fig. S21), but the mechanism is non-gravitational due to imperfect size winding at the time of the teleportation peak (Fig. S22).

Note that in our analysis, the GUE spectrum is normalized to match the operator norm of the SYK model. Additionally, the number of sizes ℓ that receive nonzero support varies for the learned, SYK, and GUE Hamiltonians due to the number of terms and presence of symmetries/constraints in each model.

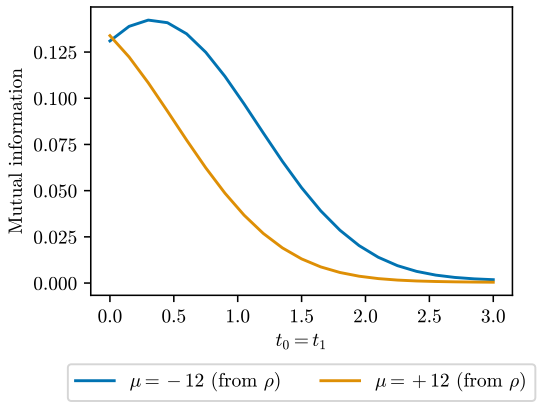

FIG. S21. The teleportation protocol evaluated with the GUE Hamiltonian at $\beta = 4$. Due to imperfect size winding, an asymmetry is observed with respect to the sign of μ; this asymmetry is significantly smaller than that of the SYK model and learned Hamiltonian.

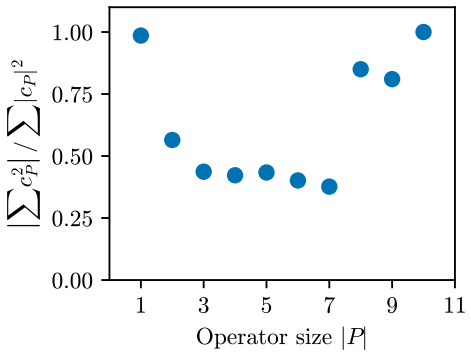

FIG. S22. Ratio of winding size distribution to the conventional size distribution at $\beta = 4$ and $t = 0.4$, i.e., the time of the teleportation peak (see Fig. S21).

IV. LEARNING NOVEL SYSTEMS

To construct a sparse SYK model that preserved the physics of a standard SYK model, we chose a loss function based only on the error from the asymmetric mutual information signature of a traversable wormhole and on a regularization penalty to induce sparsity. This procedure yielded the Hamiltonian in the main text as an instance within a larger ensemble of Hamiltonians. A 6-term instance of the same ensemble is

$$\begin{aligned} H_{L,R} = &-0.35\psi^1\psi^2\psi^3\psi^6 + 0.11\psi^1\psi^2\psi^3\psi^8 \\ &- 0.17\psi^1\psi^2\psi^4\psi^7 - 0.67\psi^1\psi^3\psi^5\psi^7 \\ &+ 0.38\psi^2\psi^3\psi^6\psi^7 - 0.05\psi^2\psi^5\psi^6\psi^7, \end{aligned} \tag{S16}$$

which, unlike the Hamiltonian in the main text, does not have all commuting terms. It successfully preserves the mutual information dynamics (Fig. S23), demonstrating perfect size winding (Fig. S24), and is consistent with other gravitational signatures.

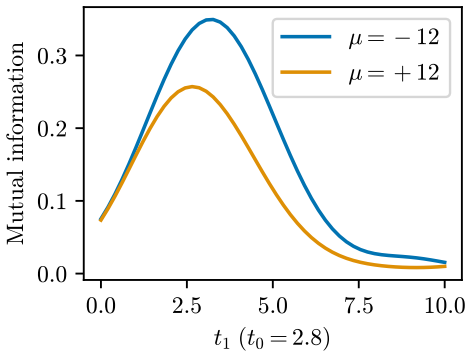

FIG. S23. Mutual information of the Hamiltonian given in Eq. S16.

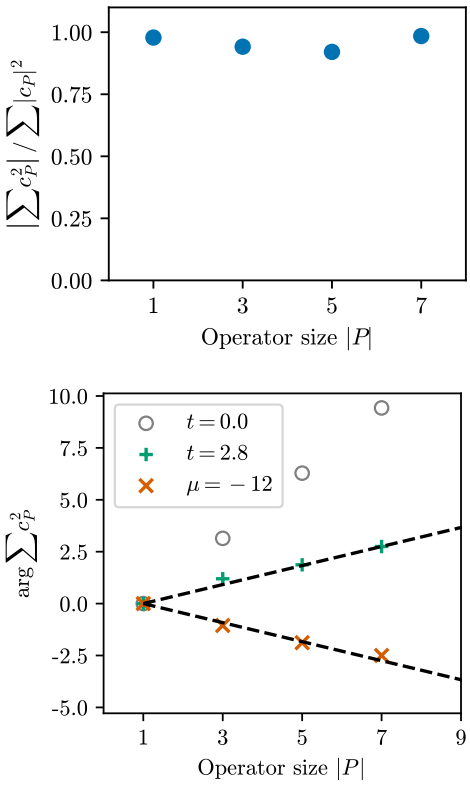

FIG. S24. Top: ratio of winding size distribution to the conventional size distribution. A value of one demonstrates perfect size winding. Bottom: the linear dependence of $q(l)$ on operator size and the action of the interaction at $\mu = -12$ shows that perfect size winding causes teleportation. The black dashed line shows equal magnitude of slope but with opposite sign, indicating $\mu = -12$ is the optimal interaction strength.

In this section, we focus on a loss function designed to optimize for new physics. We learn a Hamiltonian with a teleportation signal larger than that of the SYK model by maximizing the difference in mutual information between $\mu < 0$ and $\mu > 0$ for $I_{PT}(t_0 = t_1)$ dynamics.

Optimization produces an $N = 10$ Hamiltonian

with 8 terms:

$$\begin{aligned} H_{L,R} = &\, 0.60\psi^1\psi^3\psi^4\psi^5 + 0.72\psi^1\psi^3\psi^5\psi^6 \\ &+ 0.49\psi^1\psi^5\psi^6\psi^9 + 0.49\psi^1\psi^5\psi^7\psi^8 \\ &+ 0.64\psi^2\psi^4\psi^8\psi^{10} - 0.75\psi^2\psi^5\psi^7\psi^8 \\ &+ 0.58\psi^2\psi^5\psi^7\psi^{10} - 0.53\psi^2\psi^7\psi^8\psi^{10}. \end{aligned} \tag{S17}$$

Applying an interaction with coupling $\mu \approx -17$ is found to cause a peak in the mutual information at $t_0 = t_1 \approx 2.0$. The asymmetric mutual information with respect to $\pm\mu$ is seen to hold for both teleportation with $t_0 = t_1$ and fixed t_0, achieving a higher peak than the SYK model (Fig. S25).

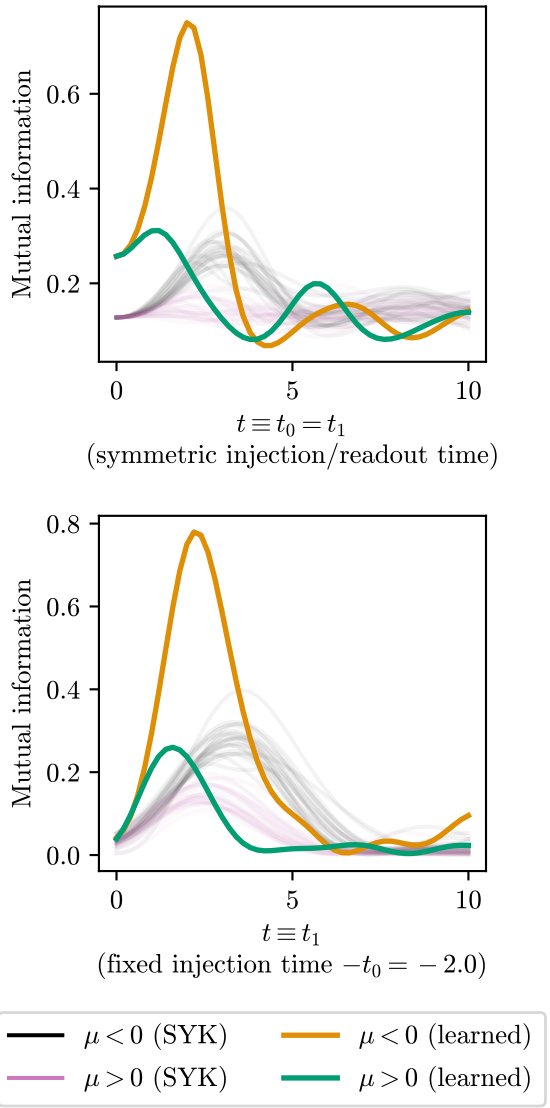

FIG. S25. Mutual information of multiple $N = 10$ SYK models (black and purple, $\beta = 4$) and learned Hamiltonians optimized for large mutual information (orange and green) showing exaggerated asymmetry in coupling with $\mu < 0$ (wormhole teleportation) and $\mu > 0$ (scrambling teleportation).

We may evaluate if the stronger teleportation signal of the novel Hamiltonian provides an experimental benefit. The Hamiltonian has approximately twice the number of terms and slightly more qubits than the Hamiltonian of the main text ($N = 5$ with 5 terms). Since the number of gates required to perform Trotterization scales linearly in the number of terms, the gate count to implement the Hamiltonian must at least double. As seen in Fig. S25, the asymmetry in mutual information between $\mu < 0$ and $\mu > 0$ increased by a factor of two. Since circuit fidelity exponential exponentially decays with respect to gate count under a depolarization noise model and the experimentally measured fidelity is already below 1/2 of the noiseless fidelity, the teleportation signal of the novel Hamiltonian will be multiplied by a factor significantly smaller than 1/2. Consequently, we find that the novel Hamiltonian cannot provide a stronger teleportation signal when experimentally measured. Generically, the above methodology may provide a useful mechanism to learn experimentally useful Hamiltonians; from a theoretical perspective, the application of machine learning to learn Hamiltonians with a given set of properties offers a computational probe that generates systems of independent interest. We proceed to verify that the learned Hamiltonian shares gravitational properties of the SYK model.

We observe that the thermalization and scrambling dynamics are similar to the initial SYK model whose coefficients initialized training. The short-time and long-time dynamics (Fig. S26) confirm that no periodicities are present despite the small number of terms in the Hamiltonian.

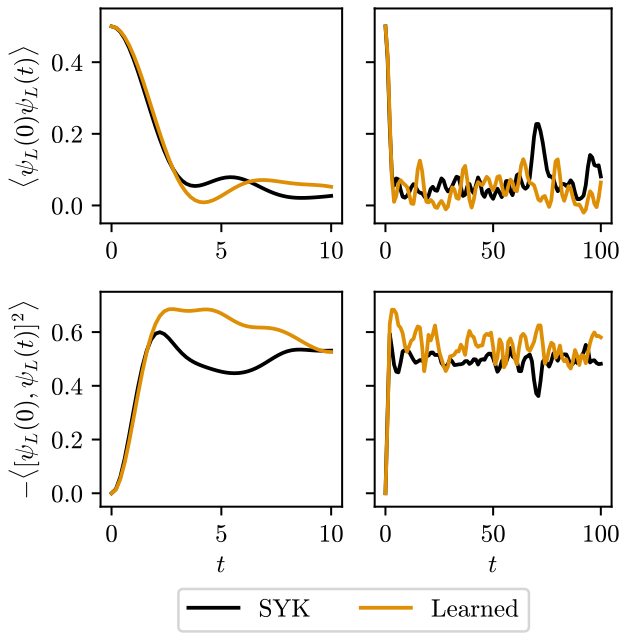

FIG. S26. Thermalization (top) and scrambling (bottom) dynamics on short (left) and long (right) time scales.

Finally, we examine the size winding behavior of the learned Hamiltonian (Fig. S27). We find a consistently large ratio between the winding size distribution and the conventional size distribution, suggesting

slightly damped size winding. As predicted by Fig. 1 of [13], we observe that the slope of $\arg q(l)$ is steeper before teleportation; at the teleportation time, the winding slows down; after the interaction, the slope reverses sign.

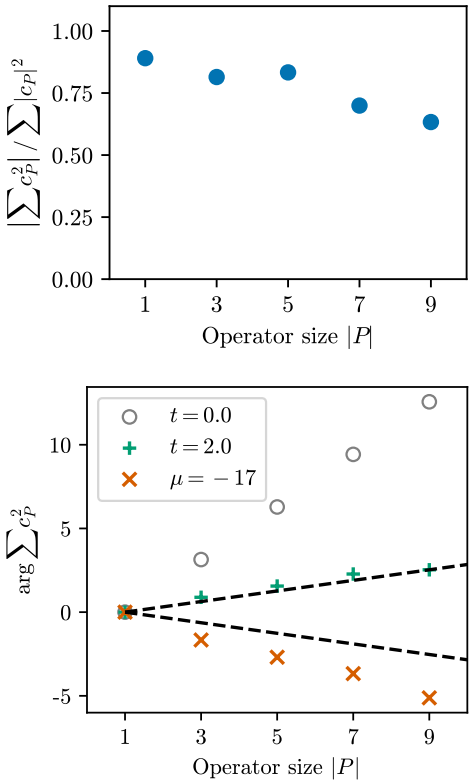

FIG. S27. Top: ratio of winding size distribution to the conventional size distribution. A value of one demonstrates perfect size winding. Bottom: the linear dependence of $q(l)$ on operator size and the action of the interaction at $\mu = -17$ shows that the infalling particle crosses the horizon. The black dashed line show a linear fit of the phases at $t = 2.0$ and a reflection with slope of equal magnitude but opposite sign.

In the main text, we apply a Trotterized interaction to demonstrate causal time-ordering. This is a simplification of the eternal traversable wormhole protocol by Maldacena and Qi [9], which we now explicitly confirm for the $N = 10$ learned Hamiltonian. Unlike in the protocol of Ref. [7], the eternal traversable wormhole replaces the instantaneous interaction $e^{i\mu V}$ at $t = 0$ with continuous time evolution under the interaction. Specifically, let

$$H_{\text{tot}} = H_L + H_R + \mu_{\text{MQ}} H_{\text{int}} \tag{S18}$$

where $H_{\text{int}} \equiv i \sum_j \psi_L^j \psi_R^j$ is the interaction operator. Time evolution is now performed under $e^{-iH_{\text{tot}}t}$ instead of $e^{-i(H_L+H_R)t}$.

We define two variant protocols and apply them using the learned Hamiltonian. In variant A, we time evolve using H_{tot} from the injection time $-t_0$ until the arrival time t_1, where the signal is said to arrive when the mutual information is maximal. The Trotterization of this time evolution is a generalization of the procedure we used in subsection I D to exhibit the causal time ordering of the traversable wormhole. The mapping of this variant protocol to the parameters of the protocol of Ref. [7] is then: $\mu_{\text{MQ}}\, t_{\text{transit}} = -\mu/(qN)$ where the transit time t_{transit} denotes the difference of the arrival and injection times. In this mapping between protocols, μ_{MQ} is a function of t_0.

Alternatively we can define a second variant protocol B, where μ_{MQ} is just some constant, and there is no direct mapping to the protocol of Ref. [7].

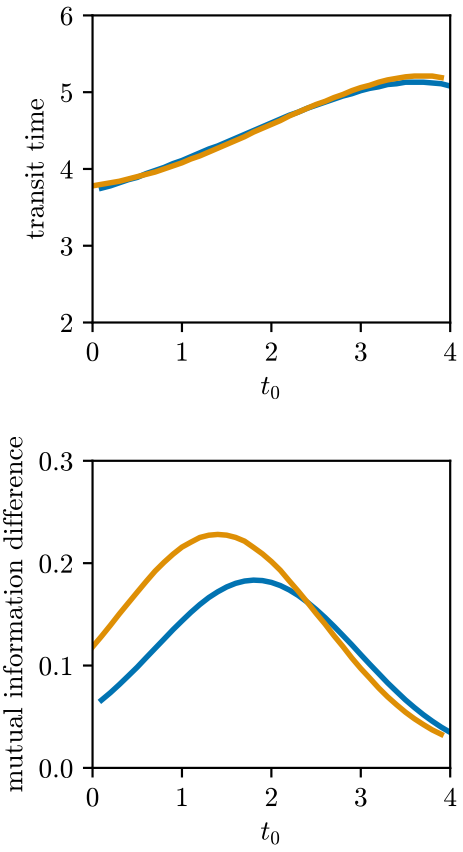

FIG. S28. Top: transit time as a function of the magnitude t_0 of the injection time, using the variant protocols A (orange) and B (blue) defined in the text. Bottom: the asymmetry in the mutual information between negative and positive values of μ_{MQ} plotted for variant protocols A (orange) and B (blue).

For both variant protocols, t_{transit} and the peak value of the mutual information are dynamically determined functions of t_0, since the TFD state is not an eigenstate of H_{tot}. We can examine, however, to what extent these variant protocols approximate the "eternal" limit, where both t_{transit} and the peak value of the mutual information become independent of t_0. Figure S28 shows the transit time as a function of t_0 obtained using protocol A, as well as protocol B

with $\mu_{\rm MQ}$ fixed to the value 0.0887. The fact that the slope of this curve is less than 1 indicates that we have causal time ordering as expected for wormhole teleportation; in the eternal wormhole limit this slope would go to zero. The variant protocols produce shallow slopes. The figure also shows that teleportation using the variant protocols produces an asymmetry in the peak values of the mutual information depending on the sign of $\mu_{\rm MQ}$, as expected for wormhole teleportation; in the eternal limit these peak values would become independent of t_0.

V. HARDWARE IMPLEMENTATION

A. Circuit decomposition

For clarity, we summarize the number of fermions and qubits required for the quantum simulation. The sparsification reduced an $N = 10$ SYK model to a sparse $N = 7$ SYK model. To encode 7 Majorana fermions on the left system and 7 Majorana fermions on the right system, we require 7 qubits (two fermions per qubit). The wormhole teleportation protocol also introduces a pair of entangled qubits, i.e., a reference qubit that is entangled with the injected qubit. Consequently, the total circuit has 9 qubits.

Each of the Majorana fermions in the Hamiltonian is encoded in a digital quantum processor via the standard Jordan-Wigner transformation to Pauli strings. Specifically, Majorana fermions are transformed to the form $\frac{1}{\sqrt{2}}Z^{\otimes k}X$ or $\frac{1}{\sqrt{2}}Z^{\otimes k}Y$ for $k \in [1, N]$. The choice of the mapping between each $\psi^i_{L,R}$ and each Pauli string is optimized to minimize the required number of two-qubit gates to perform the wormhole teleportation protocol. The particular choice of $\psi^1_R = \frac{1}{\sqrt{2}}X, \psi^2_R = \frac{1}{\sqrt{2}}Y, \psi^1_L = \frac{1}{\sqrt{2}}ZX, \psi^2_L = \frac{1}{\sqrt{2}}ZY$ ensures that the decomposition of Majorana swap gates into two-qubit gates is efficient.

To swap a qubit into or out of the wormhole, we pair up Majorana fermions on a single qubit into a Dirac fermion $\chi = \frac{1}{2}(Z^{\otimes k}X + iZ^{\otimes k}Y)$. The swap gate is then given by

$$\mathrm{SWAP} = \begin{bmatrix} \chi\chi^\dagger & \chi^\dagger \\ \chi & \chi^\dagger\chi \end{bmatrix}. \tag{S19}$$

To reduce the number of two-qubit gates, we restrict our attention to Jordan-Wigner transforms that only swap into or out of $X + iY$ and $ZX + iZY$. Since the $X + iY$ Majorana swap coincides with the standard swap given by Eq. S20, the final swap in the protocol from R to T (Fig. 1c of the main text) is replaced by direct measurement of the rightmost qubit of R to further reduce gate count. Explicitly, both swap operators are given by

$$\mathrm{SWAP}_{X+iY} = \begin{bmatrix} 1 & 0 & 0 & 0 \\ 0 & 0 & 1 & 0 \\ 0 & 1 & 0 & 0 \\ 0 & 0 & 0 & 1 \end{bmatrix} \tag{S20}$$

$$\mathrm{SWAP}_{ZX+iZY} = \begin{bmatrix} 1 & 0 & 0 & 0 & 0 & 0 & 0 & 0 \\ 0 & 0 & 1 & 0 & 0 & 0 & 0 & 0 \\ 0 & 1 & 0 & 0 & 0 & 0 & 0 & 0 \\ 0 & 0 & 0 & 1 & 0 & 0 & 0 & 0 \\ 0 & 0 & 0 & 0 & 1 & 0 & 0 & 0 \\ 0 & 0 & 0 & 0 & 0 & 0 & -1 & 0 \\ 0 & 0 & 0 & 0 & 0 & -1 & 0 & 0 \\ 0 & 0 & 0 & 0 & 0 & 0 & 0 & 1 \end{bmatrix}, \tag{S21}$$

which can be easily decomposed into either the normal swap gate (for SWAP_{X+iY}) or a series of two-qubit gates over three qubits (for SWAP_{ZX+iZY}).

Since the interaction term $V = \frac{1}{qN}\sum_j \psi^j_L\psi^j_R$ requires the exponentiation of pairs of Majorana fermions $\sum_i \psi^j_L\psi^j_R$, we further restrict the set of remaining transformations to satisfy $\psi^j_R\psi^j_L = \frac{i}{2}Z$ for a shallow Trotterization of $e^{i\mu V}$. The final degrees of freedom in choosing the Jordan-Wigner transformation are iteratively searched over to construct the most efficient implementation of the teleportation protocol on the grid architecture of the Google Sycamore processor.

The interaction term $e^{i\mu V}$ and all time evolutions e^{-iHt} are performed to first order with a single Trotter step [16]. The Trotterization does not introduce significant error compared to exact exponentiation (Fig. S30).

The chosen Jordan-Wigner transformation is as follows, where Z^i indicates $Z \otimes \cdots \otimes Z$ over i Paulis:

$$\begin{aligned} \psi^1_L &= ZX & \psi^1_R &= X \\ \psi^2_L &= ZY & \psi^2_R &= Y \\ \psi^3_L &= Z^5X & \psi^3_R &= Z^5Y \\ \psi^4_L &= Z^2X & \psi^4_R &= Z^2Y \\ \psi^5_L &= Z^4X & \psi^5_R &= Z^4Y \\ \psi^6_L &= Z^3X & \psi^6_R &= Z^3Y \\ \psi^7_L &= Z^6X. & \psi^7_R &= Z^6Y. \end{aligned} \tag{S22}$$

To prepare the TFD state, we apply a hardware-efficient variational quantum eigensolver (VQE) [17] to the Hamiltonian $H_{\rm TFD} = H_L + H_R + i\nu V$ where V is the usual coupling operator. The ground state of $H_{\rm TFD}$ is approximately the thermofield double state with inverse temperature $O(1/\nu)$ [9, 18]. With the selected Jordan-Wigner transform of Eq. S22, a variational ansatz with 13 CZ gates optimized to the ground state of $H_{\rm TFD}$ is found in classical simulation to provide over 99% overlap to the exact state $|\mathrm{TFD}\rangle = \frac{1}{\sqrt{Z}}\sum_n e^{-\beta E_n/2}|n\rangle_L \otimes |n\rangle_R$. While the gate parameter optimization could have been performed on the quantum device, we employ a classical simulation and use stochastic gradient descent to

recover the optimal gate parameters to minimize energy. We choose VQE to empirically demonstrate one possible route towards scalable TFD state preparation: as N increases, the exact thermal state need not be classically computed, reducing the classical memory cost to be linear in N. Although proving scaling of time with respect to N is difficult for such variational methods, similar approaches such as the product spectrum ansatz have been numerically shown to effectively approximate the TFD state in a scalable manner [19]. Preparing the TFD state via adiabatic time evolution requires poly(N) time [20], providing a provably efficient state preparation protocol as well as providing theoretical evidence to support numerical results showing efficient scaling with N. For further discussion of scalability, see Sec. VII A.

After compiling the full circuit of the wormhole teleportation protocol, we obtain a circuit with 164 CZ gates. Since the number of Trotter steps remains constant for all times, the number of gates does not change for all $t_0, t_1 > 0$ and $\mu \neq 0$; instead, the single-qubit rotations are reparameterized. Consequently, the amount of noise in the circuit is largely independent of the time evolution. As information scrambles over the coupled SYK models, the effect of perturbations to the noiseless state on the final teleportation mutual information may increase.

B. Calibration

We perform XEB calibration [21] of single-qubit phased XZ gates and two-qubit controlled Z gates [22]. The phased XZ gate is given by $Z^z Z^a X^x Z^{-a}$ for standard Paulis

$$X = \begin{pmatrix} 0 & 1 \\ 1 & 0 \end{pmatrix}, \qquad Z = \begin{pmatrix} 1 & 0 \\ 0 & -1 \end{pmatrix}, \tag{S23}$$

and the CZ gate is the standard gate

$$CZ = \begin{pmatrix} 1 & 0 & 0 & 0 \\ 0 & 1 & 0 & 0 \\ 0 & 0 & 1 & 0 \\ 0 & 0 & 0 & -1 \end{pmatrix}. \tag{S24}$$

By applying non-conflicting subsets of two-qubit gates simultaneously — consequently including crosstalk errors — and randomizing single-qubit gates to form a "cycle," the CZ error can be measured. We adhere to previously used calibration techniques to infer gate parameters; details for calibration can be found in [21] and the supplementary information of [22]. The resulting errors are summarized in Table I and individually reported in Fig. S29. In general, errors can include coherent and incoherent sources of noise; in simulations, we assume fully incoherent errors and observe agreement with experimental data. The mean XEB error per cycle (i.e., 2 one-qubit gates and 1 two-qubit gate) is $e_{p,\text{cycle}} \approx 0.5\%$, which represents state-of-the-art error rates on the Google Sycamore chip (cf. $e_{p,\text{cycle}} \approx 1\%$ in Refs. [22, 23] and $e_{p,\text{cycle}} \approx 0.8\%$ in Refs. [24, 25]).

Qubits are selected to minimize CZ error and to have minimal idling error. We measure the T2* decay using a Ramsey experiment, preparing a state with $\sqrt{Y}$ and measuring the expectation of X and Y operators after increasing periods of idle time. In the wormhole protocol implementation, idle time is filled with spin echo sequences if a sufficiently long gap appears in the circuit. For a discussion of measurements that minimize the impact of coherent errors, see Sec. V D below.

Gate	XEB Error
Phased XZ	$5.8\ [5.2, 7.2]\ \times 10^{-4}$
CZ	$3.4\ [2.6, 4.2]\ \times 10^{-3}$

TABLE I. Median [25th, 75th pctl.] error of gates inferred from XEB benchmarking, reported from calibration data over all gates used in the 9-qubit circuits implementing Fig. 4 of the main text.

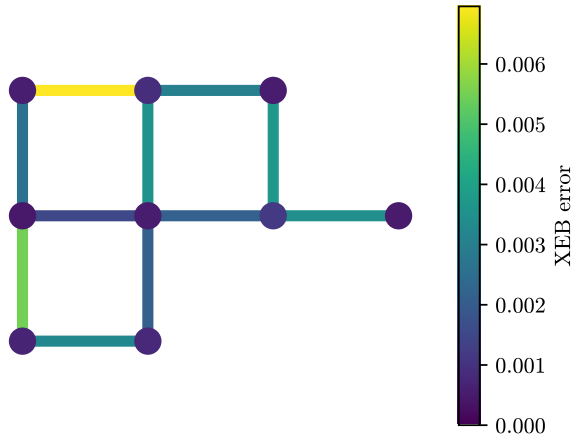

FIG. S29. XEB errors of Phased XZ gates and CZ gates over 9-qubit region used to collect data of $I_{PT}(t_1)$ for fixed t_0 in Fig. 4 of the main text.

C. Noisy simulation

To perform the noisy simulation, we assume a depolarizing noise channel $\rho \to (1-e)\rho + e\rho_{\text{mix}}$ for maximally mixed state ρ_{mix} and depolarization error e determined by calibration data. As described in Sec. V of [21], the XEB error is converted to a depolarization error e by dividing by the appropriate rescaling factor: $(1 - 1/D^2)$ for average error and $(1 - 1/D)$ for Pauli error, given Hilbert space dimension D. Applying the XEB calibration errors on a gate-by-gate basis and including idling error produces the reported noisy simulation. Simulation is performed in qsim [26] using quantum trajectories implemented by sampling Kraus operators K_i with probability $p_i = \langle\Psi| K_i^\dagger K_i |\Psi\rangle$. Written in terms of

Kraus operators, the single-qubit depolarizing channel maps $\rho \to \sum_{i=0}^{3} K_i \rho K_i^\dagger$ for $K_i = \sqrt{e} P_i/2$ and Paulis $P_i \in \{X, Y, Z\}$, and $K_0 = \sqrt{1-3e/4} I$ for the identity. After performing a Schrödinger simulation of the full statevector transformed under such operators for r trajectories, the statistical error on a resulting observable goes like $1/\sqrt{r}$. To speed up the classical simulation, computation of $\langle\Psi| K_i^\dagger K_i |\Psi\rangle$ can be probabilistically deferred and gate fusion can be applied; in the case of weak noise as observed in Table I, this significantly reduces simulation runtime [27].

D. Measurement

The mutual information $I_{PT}(t)$ may be computed in terms of von Neumann or Rényi entropy. We choose the second Rényi entropy for the quantum experiment and classical simulations associated with experimental results, while all simulation results reported above use the von Neumann entropy. The second Rényi entropy $S^{(2)} = -\log \mathrm{tr}\, \rho^2$ of a given density matrix ρ may be estimated by averaging over the tensor product of single-qubit Haar-random unitaries in the context of random measurement. Equivalently, one may perform random single-qubit Pauli measurements [25, 28]. Explicitly, the relevant quantity for $S^{(2)}$ is given by summing over measured bitstrings

$$\mathrm{tr}\, \rho^2 = 2^n \sum_{s,s'} (-2)^{-H(s,s')} \overline{P(s)P(s')} \tag{S25}$$

where H denotes Hamming distance and we have $n = 1$ or $n = 2$ qubits (P, T, or both P and T). Since only 3^2 measurements are required to perform all Pauli measurements, we do all Pauli measurements instead of randomly sampling. Note that the procedure remains efficient even for larger Hamiltonians, since the teleportation protocol only requires the input and output qubits to be measured.

To calibrate readout errors with unknown bit flip probabilities $P_{0\to1}$ and $P_{1\to0}$, we use regularized matrix inversion constrained to physical outcomes [29]. Explicitly, define a response matrix R with matrix elements given by noisy measurement probabilities $R_{ij} = \Pr(\text{noisy meas. } i | \text{noiseless meas. } j)$, where indices denote bitstring outcomes. In the absence of readout errors, R over qubits PT is a 4×4 identity matrix. A noisy measurement vector m is naively translated into an estimate $\hat{t}$ of the vector of noiseless measurements t via $\hat{t} = R^{-1} m$. However, to ensure a physical outcome without violating the set of constraints $C = \{\hat{t}_i \geq 0, \hat{t}_i \leq ||t||_1\}$, we choose

$$\hat{t} = \underset{t':C}{\mathrm{argmin}} ||m - Rt'||. \tag{S26}$$

While more sophisticated unfolding techniques are possible, the simpler approach was empirically seen to provide sufficiently stable mitigation on the small system size of 2 measured qubits. The readout errors in the response matrix are straightforwardly determined by evaluating calibration circuits with X gates on the qubits that require measurement in the teleportation circuit.

On the device, coherent errors exhibit time-dependence on the scale of 15 minutes [30]. To minimize the effect of these time-dependent errors in comparing the behavior of $\mu > 0$ and $\mu < 0$, circuits are evaluated in an interlaced fashion. Collecting data consists of 10,000 measurements of each of the nine Pauli bases required to compute mutual information, completed for all values of t in the mutual information plot of a given value of μ. These circuits are evaluated by sweeping over parameters with a fixed t and fixed Pauli basis, but doing back-to-back measurements of 10,000 $\mu > 0$ samples followed by 10,000 $\mu < 0$ samples. Since one round of 10,000 measurements takes only a few seconds, positive and negative values of μ are subject to approximately the same time-dependent noise. A series of $(90,000 \text{ measurements}) \times$ (15 values of t) $\times$ (2 values of μ) consists of one run. Multiple runs in this manner (e.g., 28 runs for $t_0 = 2.8$ and varying t_1) provide a mean mutual information with error bars; this procedure thus averages over time-dependent errors.

VI. ADDITIONAL EXPERIMENTAL DATA

A. Mutual information dynamics

The scrambling of the Majorana fermion across the left system must be exactly replicated by the scrambling dynamics that refocus the Majorana fermion in the right system, causing the teleportation protocol to be sensitive to errors. Adding a depolarization channel may misalign such scrambling dynamics, attenuating the teleportation signal as $I_{PT}(t)$ assumes values of t on the order of the scrambling time. We confirm this behavior by the experimental measurement and noisy simulation of the mutual information $I_{PT}(t)$ for both $\mu = -12$ and $\mu = +12$ (Fig. S30). The difference between the above mutual information curves for negative and positive values of μ is reported in Fig. 4c of the main text. In Fig. S30, we also show the result of the protocol with $\mu = 0$; further discussion is provided in Sec. VI C below.

Due to the scrambling-unscrambling dynamics of the wormhole teleportation protocol, the mutual information is very sensitive to the amount of depolarizing noise. Given the gate errors reported in Sec. V B, the simulations of Fig. S30 show that the asymmetry of mutual information in μ can be resolved. As gate errors decrease, the signal rapidly improves; as errors increase, it rapidly deteriorates (Fig. S31). If gates experience 1.5x the error rate observed on the device, the asymmetry cannot be resolved with a reasonable number of measurements.

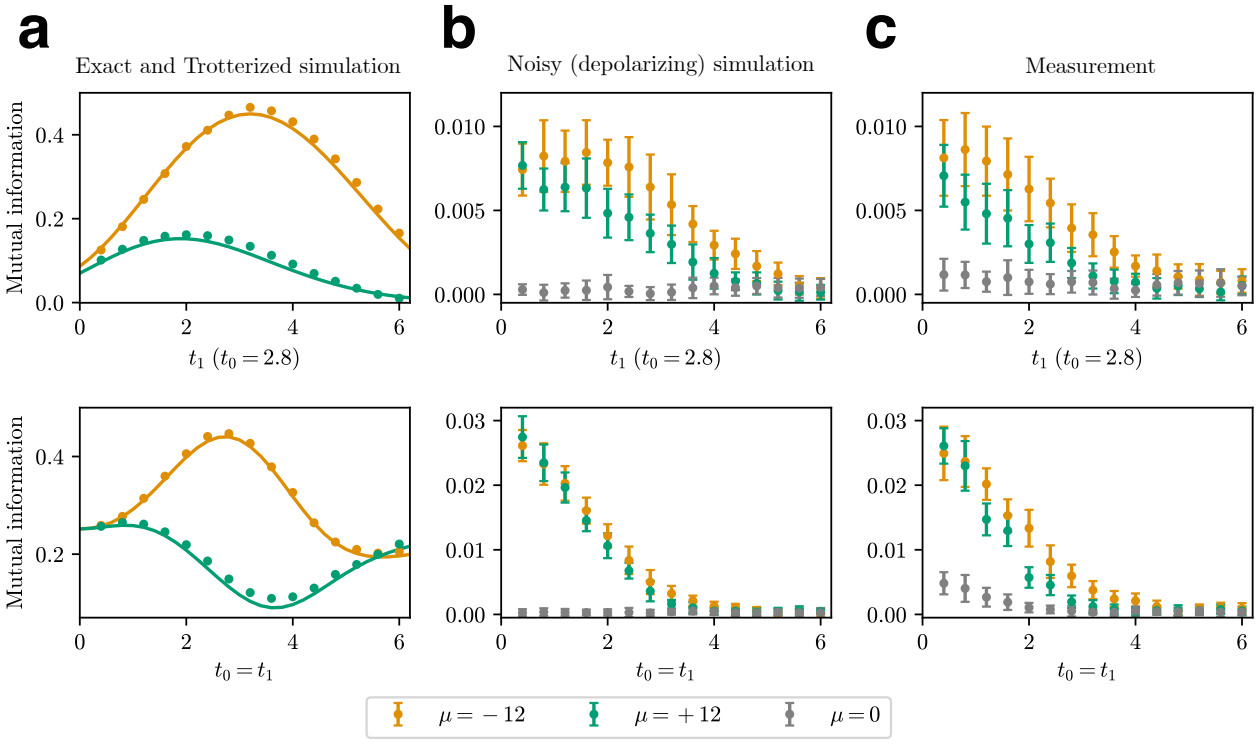

FIG. S30. **a**, Exact (solid) and circuit (dotted) simulation of the wormhole teleportation protocol. **b**, Noisy circuit simulation of the wormhole teleportation protocol. Each gate is subjected to depolarization error determined by calibration data. **c**, Observation of traversable wormhole dynamics on quantum hardware. Error bars show one standard deviation across multiple runs (28 runs, top; 20 runs, bottom). The measurements agree with noisy simulation and reproduce the sign dependence of the mutual information, consistent with through-the-wormhole teleportation. The teleportation protocol with no interaction ($\mu = 0$, 20 runs) demonstrates the presence of coherent errors, as seen by nonzero mutual information; however, the signal due to coherent error is small compared to the measured teleportation signal with $\mu \neq 0$, showing that coherent errors are minimal. Error bars in (b) and (c) show one standard deviation across all runs (90,000 measurements per run).

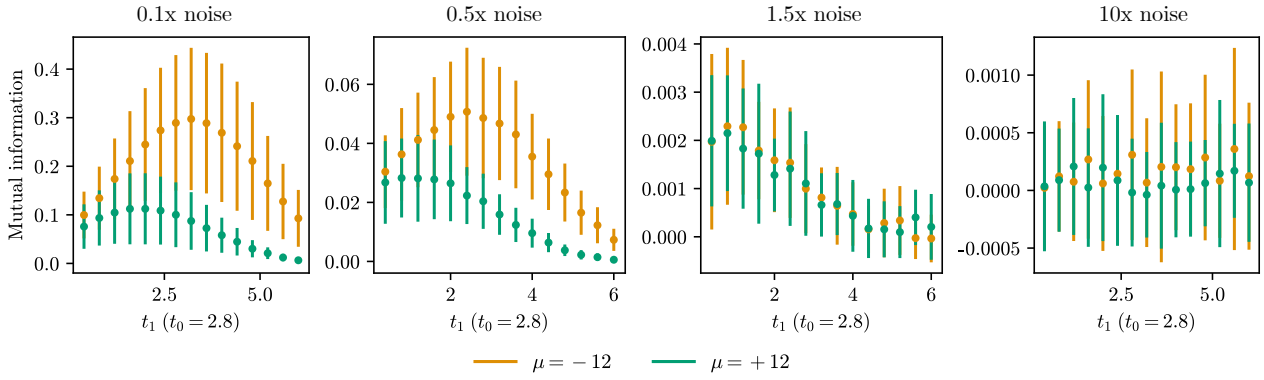

FIG. S31. Dependence of mutual information asymmetry on depolarizing noise, simulated for different multiplicative values of the probability of gate error. Due to increased scrambling with time, noise attenuates the peak. This causes noise to both reduce the separation between $\mu = \pm 12$ and shift the peak to earlier times. See Fig. S30 for simulations at the level of measured device noise (i.e., 1x noise). Reducing errors to 0.5x noise increases $I_{\mu<0} - I_{\mu>0}$ by a factor of 10, while increasing errors to 1.5x noise obscures the asymmetry.

B. Thermalization behavior

We experimentally verify the thermalization behavior of a single SYK model by measuring the mutual information between a reference qubit and an entangled qubit injected into one SYK model subjected to time evolution (Fig. S32). We retain the choice of Jordan-Wigner transformation from Majorana fermions to individual qubits, as well as the variational TFD state preparation at the beginning of the protocol to remain

consistent with the noise present in the main experiment. The standard swap gate of Eq. S20 holds for the right SYK system, allowing the final swap gate to T in Fig. S32 to be replaced by a direct measurement on the rightmost qubit of R. The final circuit requires 109 two-qubit gates.

Under a depolarization model of noise given by calibration data and assuming an idle qubit error value of 0.3 times the corresponding single-qubit gate depolarization error, we experimentally observe that the measured thermalization agrees with noisy simulation (Fig. S33). The figure replicates Fig. 4a of the main text, but it also includes the exact simulation in the absence of noise.

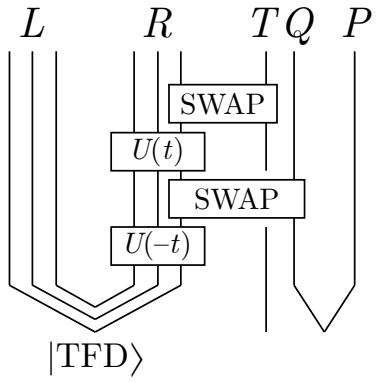

FIG. S32. Protocol to measure thermalization behavior. One qubit in a Bell pair is swapped into the right SYK system at time $-t$, then the corresponding fermion is recovered at time 0; thermalization is measured by the quantity $I_{PT}(t)$.

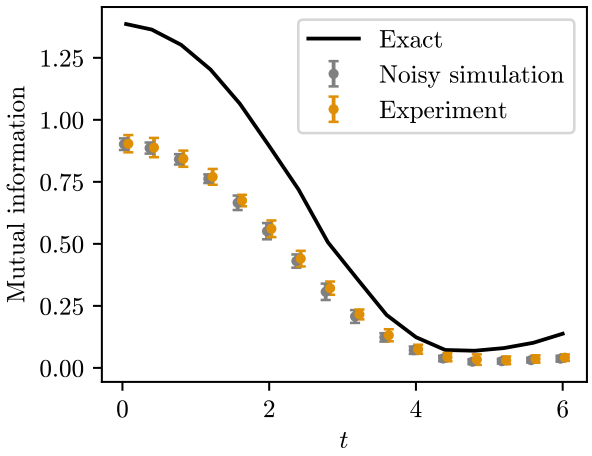

FIG. S33. Experimental measurement of thermalization. The observed mutual information dynamics are consistent with thermalization and closely match noisy simulations assuming only a depolarizing channel. Error bars show 3 standard deviations from 20 runs. For visual clarity, the noisy simulations and experimental data are horizontally offset from one another.

C. Mutual information without interaction

We evaluate the background teleportation signal induced by coherent errors independent of the teleportation protocol.

All noisy simulations only assume depolarizing noise, but errors such as crosstalk (see Fig. S9 of [23]) and phase errors (see Fig. S2 of [30]) can cause coherent errors that reduce the mutual information due to misalignment between scrambling in the left and right systems. The Jordan-Wigner transformation of Eq. S22 does not spatially separate the left and right systems on the device, and thus coherent errors may also cause the left and right systems to interact, for example during the time evolution of the left or right systems. Removing the interaction reduces the circuit gate count from 164 CZ gates to 163 CZ gates since $e^{i\mu V}$ is largely comprised of single-qubit gates.

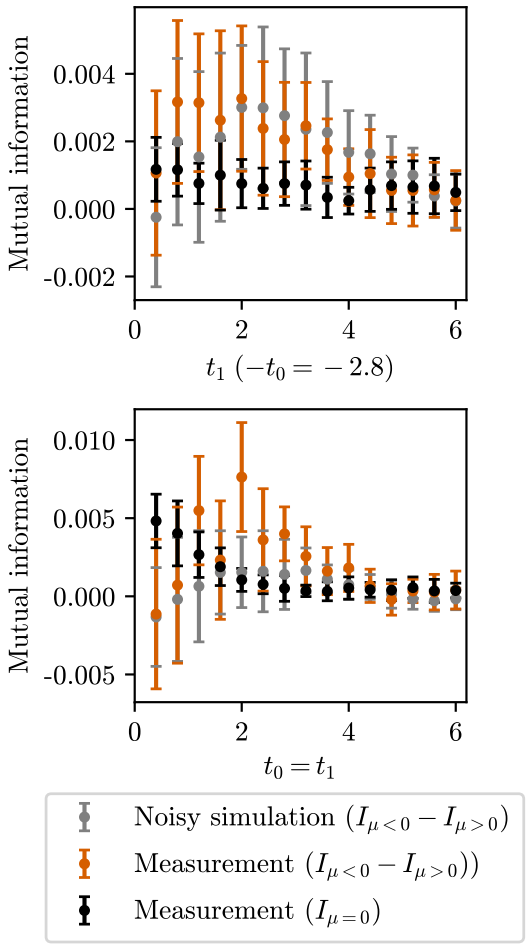

FIG. S34. Experimental measurement of wormhole nonteleportation protocol (i.e., $\mu = 0$) compared to the measured and simulated asymmetry in mutual information of the traversable wormhole (i.e., $I_{\mu<0} - I_{\mu>0}$, reproduced from Fig. 4 of the main text). Error bars show one standard deviation over a fixed number of runs ($\mu \neq 0$: 28 runs, top; 20 runs, bottom; $\mu = 0$: 20 runs for both top and bottom).

In the presence of only incoherent noise, the mutual information I_{PT} with $\mu = 0$ should remain time-independent and approximately zero. Measurement on the device yields slightly nonzero mutual information, but the fake signal is uncorrelated with the asymmetric signature in μ and is weaker than the traversable wormhole signal (Fig. S30). We observe that device noise is dominated by an incoherent channel, thus excluding the possibility that coherent errors mimic the traversable wormhole signal. In Fig. S34, the $\mu = 0$ mutual information is also seen to be smaller than the difference between mutual informations for $\mu = \pm 12$, confirming that the observed difference is significant compared to the size of coherent errors. For completeness, we illustrate the circuit in Fig. S35. A more careful analysis follows in the next subsection.

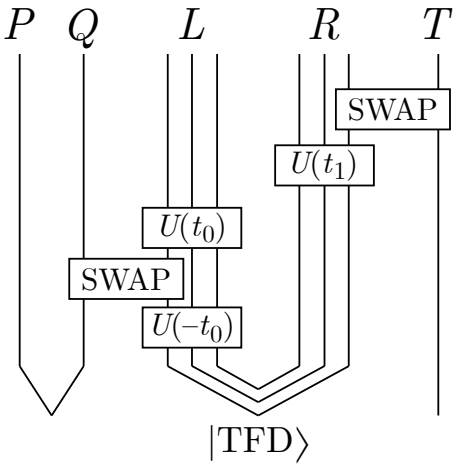

FIG. S35. Wormhole non-teleportation protocol, i.e., the teleportation protocol but without interaction ($\mu = 0$). The mutual information I_{PT} is zero at all times since the left and right sides cannot communicate information.

D. Statistical analysis

We discuss the statistical significance of the applying the interaction. Let ΔI be the difference in the mutual information in runs with $\mu = -12$ and $\mu = +12$. Considering the experiment where $t_0 = 2.8$, we compare the wormhole teleportation measurements to the reference case with no interaction ($\mu = 0$). In the absence of noise, the distribution of ΔI for $\mu = 0$ is expected to have null mean; due to coherent error, the measured distribution differs from zero. For each value of t_1, we compute the sample mean and variance and we use a t-test to evaluate the compatibility of a null expected value (Fig. S36).

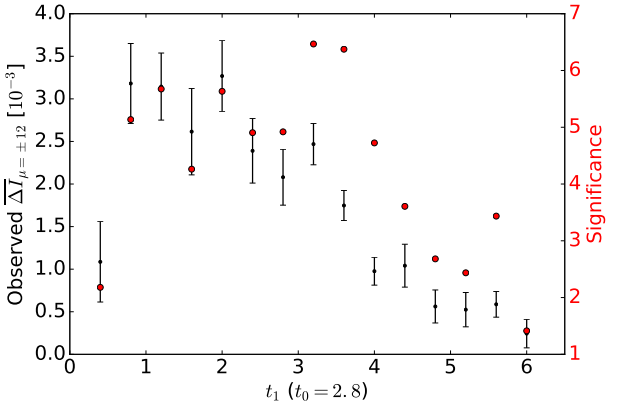

FIG. S36. Black: the sample mean and standard error of $I_{\mu=-12} - I_{\mu=+12}$. Red: the statistical significance of the separation from $I_{\mu=0}$ in units of σ.

VII. OUTLOOK

This work is a first point of contact between quantum gravity and experimental on-chip quantum processing [12, 13, 15]. We measure through-the-wormhole transmission of a qubit using a small-N sparsification of an SYK system. In the following, we discuss opportunities to expand this work at larger N. We examine additional observables that provide insight in the regime of $N = O(100)$, where quantum computers may perform experiments that cannot be simulated by classical resources.

A. Scalability

Due to the level of noise in current quantum hardware, we use machine learning in classical simulation to obtain a sparse Hamiltonian that preserves the gravitational physics of a dense SYK system. A dense SYK system with N fermions has $O(N^4)$ Hamiltonian terms for $q = 4$; our optimization reduces the number of terms up to a lower bound of $O(N)$ nonzero terms required for scrambling across the system. In the far future, one might envision optimization of Hamiltonians implemented entirely on a quantum device. Today, an efficient classical pre-processing procedure exists to produce a Hamiltonian with $O(N)$ terms that preserves gravitational physics.

In the beyond-classical regime of computation, we wish to measure an observable of an N-fermion SYK system. To scramble across all fermions, at least N/q terms are required; this provides a lower bound to the number of Hamiltonian terms in any quantum gravity experiment. Using random sparsification of a dense SYK system, it has been analytically shown in the large-N limit that gravitational physics is preserved for kN nonzero terms, where k is of order unity [31–33]. We expect then in the large-N limit that at most a multiplicative factor of $O(q)$ additional Hamiltonian terms are required by random sparsification compared

to an optimized sparsification procedure. It has been shown that for an SYK system with $N = 52$ and $q = 4$, choosing $k = 4$ is sufficiently large to preserve gravitational behavior via random sparsification [31]. Random sparsification is effective due to the expander graph properties of random graphs. A related approach using hypergraphs [32] shows similar results for k of order unity and $N = 24$ [33]. This places an upper bound on the overhead of random sparsification compared to machine learning sparsification in the beyond-classical regime, demonstrating that simulation of the sparsified SYK system requires minimal additional overhead to become efficient.

To perform further probes of wormhole dynamics, preparation of the thermofield double (TFD) state is also required. In this work, we used a variational approach to prepare the TFD state as the ground state of a known Hamiltonian [9, 18]. Variational methods are widely employed in the literature to prepare TFD states with empirical evidence of high state overlap and poly(N) scaling using the product spectrum ansatz, hardware-efficient ansatzes, and other approaches [19, 34–37]. Thermofield double state preparation via adiabatic time evolution has been shown to require poly(N) time [20], offering a provably efficient protocol as well as strong theoretical evidence to support the efficient scaling empirically observed for variational methods.

B. Benchmarking

The wormhole teleportation protocol can be used as a benchmark for beyond-classical quantum computation. The large-N solution of the SYK system demands certain features to be satisfied by the quantum simulation, notably the asymmetry in mutual information, allowing validation and verification of the circuit output. The scrambling-unscrambling dynamics dictated by the size winding description of wormhole teleportation implies strong sensitivity to coherent errors: a qubit inserted into the wormhole grows over the entire system before unscrambling on the other side. Since errors partway through the protocol prevent the qubit from traversing the wormhole, the mutual information is critically dependent on circuit fidelity (Fig. S31). Unlike scrambling protocols that measure quantities such as information spread [23], the traversable wormhole protocol offers a robust measure of fidelity.

C. Future probes

Three natural regions emerge when evaluating gravitational physics by through the interrogation of a many-body system: 1) the small-N regime, which is classically accessible; 2) the large-N regime, which is well-described by semiclassical gravity; and 3) the mesoscopic regime in between the two limits above. The most interesting regime from a gravitational system is the last one. While scattering in the large-N and low-temperature limit is completely elastic, systems in the mesoscopic region experience inelastic effects in the bulk. These stringy corrections reduce the teleportation signal, as described by the chord diagram computation discussed in this work. However, our current understanding of such inelastic effects is incomplete. Quantum computers in the near-term mesoscopic regime of $N = O(100)$ provide a tool to computationally probe the precise region where the gravitational description is least developed.

Within this regime, quantum computers provide insight into dynamics caused by a fluctuating effective time rate (i.e., time dilation) that is controlled by Shapiro delays and advances. The gravitational effect of errors in the many-body evolution are mostly Shapiro delays, suggesting that one could envision nontrivial recovery protocols. Our experiment measured the strength of teleportation through the wormhole, which is shown to be visible at N small enough to be accessible to current hardware. As quantum gate fidelities improve and larger N systems are accessible, additional observables will provide new insight into the physics of the emergent spacetime.

In the context of the SYK model, observables of the form $\psi_i \partial^n \psi_i$ are associated with towers of massive particles in the bulk, whose full description may be expressed as excitations of a string. Corrections to the elastic process of the Shapiro delay can result in inelastic production of those excitations, which could be directly measured in future experiments. Furthermore, finite-N corrections in the mesoscopic regime are associated with higher order and quantum loop corrections to gravitational scattering, as well as effects related to the particular instantiation of the couplings J. Systematic measurements in such quantum systems produce data of scattering processes in the bulk, which can be used to understand the full bulk theory. In addition to scattering type experiments in the thermofield double background, it will also be interesting to use future versions of the wormhole teleportation protocol at higher fidelity to probe the structure of the bulk states produced by variations of the TFD state [38].

[1] A. M. Garcia-Garcia and J. J. Verbaarschot, Physical Review D **94**, 126010 (2016).

[2] A. M. García-García and J. J. M. Verbaarschot, Phys.

Rev. D **96**, 066012 (2017).
[3] J. S. Cotler, G. Gur-Ari, M. Hanada, J. Polchinski, P. Saad, S. H. Shenker, D. Stanford, A. Streicher, and M. Tezuka, Journal of High Energy Physics **2017**, 118 (2017).
[4] J. Maldacena and D. Stanford, Phys. Rev. D **94**, 106002 (2016), arXiv:1604.07818 [hep-th].
[5] T. Guhr, A. Müller–Groeling, and H. A. Weidenmüller, Physics Reports **299**, 189 (1998).
[6] J. Maldacena, S. H. Shenker, and D. Stanford, Journal of High Energy Physics **2016**, 106 (2016).
[7] P. Gao and D. L. Jafferis, Journal of High Energy Physics **2021**, 97 (2021).
[8] M. Berkooz, M. Isachenkov, V. Narovlansky, and G. Torrents, JHEP **03**, 079 (2019), arXiv:1811.02584 [hep-th].
[9] J. Maldacena and X.-L. Qi, "Eternal traversable wormhole," (2018), arXiv:1804.00491 [hep-th].
[10] J. Maldacena, D. Stanford, and Z. Yang, Fortschritte der Physik **65**, 1700034 (2017).
[11] P. Gao and H. Liu, JHEP **10**, 048 (2019), arXiv:1810.01444 [hep-th].
[12] A. R. Brown, H. Gharibyan, S. Leichenauer, H. W. Lin, S. Nezami, G. Salton, L. Susskind, B. Swingle, and M. Walter, "Quantum gravity in the lab: Teleportation by size and traversable wormholes," (2021), arXiv:1911.06314 [quant-ph].
[13] S. Nezami, H. W. Lin, A. R. Brown, H. Gharibyan, S. Leichenauer, G. Salton, L. Susskind, B. Swingle, and M. Walter, "Quantum gravity in the lab: Teleportation by size and traversable wormholes, part ii," (2021), arXiv:2102.01064 [quant-ph].
[14] X.-L. Qi and A. Streicher, Journal of High Energy Physics **2019**, 12 (2019).
[15] T. Schuster, B. Kobrin, P. Gao, I. Cong, E. T. Khabiboulline, N. M. Linke, M. D. Lukin, C. Monroe, B. Yoshida, and N. Y. Yao, Phys. Rev. X **12**, 031013 (2022).
[16] H. F. Trotter, Proceedings of the American Mathematical Society **10**, 545 (1959).
[17] A. Kandala, A. Mezzacapo, K. Temme, M. Takita, M. Brink, J. M. Chow, and J. M. Gambetta, Nature **549**, 242 (2017).
[18] W. Cottrell, B. Freivogel, D. M. Hofman, and S. F. Lokhande, Journal of High Energy Physics **2019**, 58 (2019).
[19] J. Martyn and B. Swingle, Phys. Rev. A **100**, 032107 (2019).
[20] H. Gharibyan, M. Hanada, M. Honda, and J. Liu, JHEP **07**, 140 (2021), arXiv:2011.06573 [hep-th].
[21] F. Arute, K. Arya, R. Babbush, D. Bacon, J. C. Bardin, R. Barends, R. Biswas, S. Boixo, F. G. S. L. Brandao, D. A. Buell, and et al., Nature **574**, 505–510 (2019).
[22] X. Mi, M. Ippoliti, C. Quintana, A. Greene, Z. Chen, J. Gross, F. Arute, K. Arya, J. Atalaya, R. Babbush, J. C. Bardin, J. Basso, A. Bengtsson, A. Bilmes, A. Bourassa, L. Brill, M. Broughton, B. B. Buckley, D. A. Buell, B. Burkett, N. Bushnell, B. Chiaro, R. Collins, W. Courtney, D. Debroy, S. Demura, A. R. Derk, A. Dunsworth, D. Eppens, C. Erickson, E. Farhi, A. G. Fowler, B. Foxen, C. Gidney, M. Giustina, M. P. Harrigan, S. D. Harrington, J. Hilton, A. Ho, S. Hong, T. Huang, A. Huff, W. J. Huggins, L. B. Ioffe, S. V. Isakov, J. Iveland, E. Jeffrey, Z. Jiang, C. Jones, D. Kafri, T. Khattar, S. Kim, A. Kitaev, P. V. Klimov, A. N. Korotkov, F. Kostritsa, D. Landhuis, P. Laptev, J. Lee, K. Lee, A. Locharla, E. Lucero, O. Martin, J. R. McClean, T. McCourt, M. McEwen, K. C. Miao, M. Mohseni, S. Montazeri, W. Mruczkiewicz, O. Naaman, M. Neeley, C. Neill, M. Newman, M. Y. Niu, T. E. O'Brien, A. Opremcak, E. Ostby, B. Pato, A. Petukhov, N. C. Rubin, D. Sank, K. J. Satzinger, V. Shvarts, Y. Su, D. Strain, M. Szalay, M. D. Trevithick, B. Villalonga, T. White, Z. J. Yao, P. Yeh, J. Yoo, A. Zalcman, H. Neven, S. Boixo, V. Smelyanskiy, A. Megrant, J. Kelly, Y. Chen, S. L. Sondhi, R. Moessner, K. Kechedzhi, V. Khemani, and P. Roushan, Nature **601**, 531 (2022).
[23] X. Mi, P. Roushan, C. Quintana, S. Mandrà, J. Marshall, C. Neill, F. Arute, K. Arya, J. Atalaya, R. Babbush, and et al., Science **374**, 1479–1483 (2021).
[24] Z. Chen, K. J. Satzinger, J. Atalaya, A. N. Korotkov, A. Dunsworth, D. Sank, C. Quintana, M. McEwen, R. Barends, P. V. Klimov, S. Hong, C. Jones, A. Petukhov, D. Kafri, S. Demura, B. Burkett, C. Gidney, A. G. Fowler, H. Putterman, I. Aleiner, F. Arute, K. Arya, R. Babbush, J. C. Bardin, A. Bengtsson, A. Bourassa, M. Broughton, B. B. Buckley, D. A. Buell, N. Bushnell, B. Chiaro, R. Collins, W. Courtney, A. R. Derk, D. Eppens, C. Erickson, E. Farhi, B. Foxen, M. Giustina, J. A. Gross, M. P. Harrigan, S. D. Harrington, J. Hilton, A. Ho, T. Huang, W. J. Huggins, L. B. Ioffe, S. V. Isakov, E. Jeffrey, Z. Jiang, K. Kechedzhi, S. Kim, F. Kostritsa, D. Landhuis, P. Laptev, E. Lucero, O. Martin, J. R. McClean, T. McCourt, X. Mi, K. C. Miao, M. Mohseni, W. Mruczkiewicz, J. Mutus, O. Naaman, M. Neeley, C. Neill, M. Newman, M. Y. Niu, T. E. O'Brien, A. Opremcak, E. Ostby, B. Pató, N. Redd, P. Roushan, N. C. Rubin, V. Shvarts, D. Strain, M. Szalay, M. D. Trevithick, B. Villalonga, T. White, Z. J. Yao, P. Yeh, A. Zalcman, H. Neven, S. Boixo, V. Smelyanskiy, Y. Chen, A. Megrant, and J. Kelly, "Exponential suppression of bit or phase flip errors with repetitive error correction," (2021).
[25] K. J. Satzinger, Y. Liu, A. Smith, C. Knapp, M. Newman, C. Jones, Z. Chen, C. Quintana, X. Mi, A. Dunsworth, C. Gidney, I. Aleiner, F. Arute, K. Arya, J. Atalaya, R. Babbush, J. C. Bardin, R. Barends, J. Basso, A. Bengtsson, A. Bilmes, M. Broughton, B. B. Buckley, D. A. Buell, B. Burkett, N. Bushnell, B. Chiaro, R. Collins, W. Courtney, S. Demura, A. R. Derk, D. Eppens, C. Erickson, E. Farhi, L. Foaro, A. G. Fowler, B. Foxen, M. Giustina, A. Greene, J. A. Gross, M. P. Harrigan, S. D. Harrington, J. Hilton, S. Hong, T. Huang, W. J. Huggins, L. B. Ioffe, S. V. Isakov, E. Jeffrey, Z. Jiang, D. Kafri, K. Kechedzhi, T. Khattar, S. Kim, P. V. Klimov, A. N. Korotkov, F. Kostritsa, D. Landhuis, P. Laptev, A. Locharla, E. Lucero, O. Martin, J. R. McClean, M. McEwen, K. C. Miao, M. Mohseni, S. Montazeri, W. Mruczkiewicz, J. Mutus, O. Naaman, M. Neeley, C. Neill, M. Y. Niu, T. E. O'Brien, A. Opremcak, B. Pató, A. Petukhov, N. C. Rubin, D. Sank, V. Shvarts, D. Strain, M. Szalay, B. Villalonga, T. C. White, Z. Yao, P. Yeh, J. Yoo, A. Zalcman, H. Neven, S. Boixo, A. Megrant, Y. Chen, J. Kelly, V. Smelyanskiy, A. Kitaev, M. Knap, F. Pollmann, and P. Roushan, "Realizing topologically

ordered states on a quantum processor," (2021), arXiv:2104.01180 [quant-ph].
[26] Q. A. team and collaborators, "qsim," (2020).
[27] S. V. Isakov, D. Kafri, O. Martin, C. V. Heidweiller, W. Mruczkiewicz, M. P. Harrigan, N. C. Rubin, R. Thomson, M. Broughton, K. Kissell, E. Peters, E. Gustafson, A. C. Y. Li, H. Lamm, G. Perdue, A. K. Ho, D. Strain, and S. Boixo, "Simulations of quantum circuits with approximate noise using qsim and cirq," (2021), arXiv:2111.02396 [quant-ph].
[28] H.-Y. Huang, R. Kueng, and J. Preskill, Nature Physics **16**, 1050 (2020).
[29] B. Nachman, M. Urbanek, W. A. de Jong, and C. W. Bauer, npj Quantum Information **6**, 84 (2020).
[30] F. Arute, K. Arya, R. Babbush, D. Bacon, J. C. Bardin, R. Barends, A. Bengtsson, S. Boixo, M. Broughton, B. B. Buckley, D. A. Buell, B. Burkett, N. Bushnell, Y. Chen, Z. Chen, Y.-A. Chen, B. Chiaro, R. Collins, S. J. Cotton, W. Courtney, S. Demura, A. Derk, A. Dunsworth, D. Eppens, T. Eckl, C. Erickson, E. Farhi, A. Fowler, B. Foxen, C. Gidney, M. Giustina, R. Graff, J. A. Gross, S. Habegger, M. P. Harrigan, A. Ho, S. Hong, T. Huang, W. Huggins, L. B. Ioffe, S. V. Isakov, E. Jeffrey, Z. Jiang, C. Jones, D. Kafri, K. Kechedzhi, J. Kelly, S. Kim, P. V. Klimov, A. N. Korotkov, F. Kostritsa, D. Landhuis, P. Laptev, M. Lindmark, E. Lucero, M. Marthaler, O. Martin, J. M. Martinis, A. Marusczyk, S. McArdle, J. R. McClean, T. McCourt, M. McEwen, A. Megrant, C. Mejuto-Zaera, X. Mi, M. Mohseni, W. Mruczkiewicz, J. Mutus, O. Naaman, M. Neeley, C. Neill, H. Neven, M. Newman, M. Y. Niu, T. E. O'Brien, E. Ostby, B. Pató, A. Petukhov, H. Putterman, C. Quintana, J.-M. Reiner, P. Roushan, N. C. Rubin, D. Sank, K. J. Satzinger, V. Smelyanskiy, D. Strain, K. J. Sung, P. Schmitteckert, M. Szalay, N. M. Tubman, A. Vainsencher, T. White, N. Vogt, Z. J. Yao, P. Yeh, A. Zalcman, and S. Zanker, "Observation of separated dynamics of charge and spin in the fermi-hubbard model," (2020), arXiv:2010.07965 [quant-ph].
[31] S. Xu, L. Susskind, Y. Su, and B. Swingle, "A sparse model of quantum holography," (2020), arXiv:2008.02303 [cond-mat.str-el].
[32] A. M. Garcia-Garcia, Y. Jia, D. Rosa, and J. J. M. Verbaarschot, Phys. Rev. D **103**, 106002 (2021).
[33] E. Caceres, A. Misobuchi, and R. Pimentel, JHEP **11**, 015 (2021), arXiv:2108.08808 [hep-th].
[34] J. Wu and T. H. Hsieh, Phys. Rev. Lett. **123**, 220502 (2019).
[35] D. Zhu, S. Johri, N. M. Linke, K. A. Landsman, C. H. Alderete, N. H. Nguyen, A. Y. Matsuura, T. H. Hsieh, and C. Monroe, Proceedings of the National Academy of Sciences **117**, 25402 (2020), https://www.pnas.org/doi/pdf/10.1073/pnas.2006337117.
[36] V. P. Su, Phys. Rev. A **104**, 012427 (2021).
[37] R. Sagastizabal, S. P. Premaratne, B. A. Klaver, M. A. Rol, V. Negîrneac, M. S. Moreira, X. Zou, S. Johri, N. Muthusubramanian, M. Beekman, C. Zachariadis, V. P. Ostroukh, N. Haider, A. Bruno, A. Y. Matsuura, and L. DiCarlo, npj Quantum Information **7**, 130 (2021).
[38] L. Susskind, "Dear qubitzers, gr=qm," (2017), arXiv:1708.03040 [hep-th].